Materials Today Bio 26 (2024) 101078

Contents lists available at ScienceDirect

Materials Today Bio

journal homepage: www.journals.elsevier.com/materials-today-bio

A sponge-like nanofiber melatonin-loaded scaffold accelerates vascularized bone regeneration via improving mitochondrial energy metabolism

Nanning Lv [a,d,e,1], Mingzhuang Hou [a,b,1], Lei Deng [a,b,1], Xi Hua [a,b], Xinfeng Zhou [a,b], Hao Liu [a,b], Xuesong Zhu [a,b], Yong Xu [a,b], Zhonglai Qian [a,b], Qing Li [c,**], Mingming Liu [d,e,***], Fan He [a,b,c,*]

[a] Department of Orthopaedics, The First Affiliated Hospital of Soochow University, Soochow University, Suzhou, 215006, China
[b] Orthopaedic Institute, Suzhou Medical College, Soochow University, Suzhou, 215000, China
[c] Department of Pathology, The Third Affiliated Hospital of Soochow University, Changzhou, 213003, China
[d] Department of Orthopaedics, The Affiliated Lianyungang Clinical College of Xuzhou Medical University, Lianyungang, 222003, China
[e] Department of Orthopaedics, Lianyungang Second People's Hospital Affiliated to Kangda College of Nanjing Medical University, Lianyungang, 222003, China

ARTICLE INFO

Keywords:
Electrospun
Melatonin
Nanofiber scaffolds
Bone marrow mesenchymal stem cells
Mitochondrial function
Critical-sized bone defects

ABSTRACT

Electrospun nanofibers have been widely employed in bone tissue engineering for their ability to mimic the micro to nanometer scale network of the native bone extracellular matrix. However, the dense fibrous structure and limited mechanical support of these nanofibers pose challenges for the treatment of critical size bone defects. In this study, we propose a facile approach for creating a three-dimensional scaffold using interconnected electrospun nanofibers containing melatonin (Scaffold@MT). The hypothesis posited that the sponge-like Scaffold@MT could potentially enhance bone regeneration and angiogenesis by modulating mitochondrial energy metabolism. Melatonin-loaded gelatin and poly-lactic-acid nanofibers were fabricated using electrospinning, then fragmented into shorter fibers. The sponge-like Scaffold@MT was created through a process involving homogenization, low-temperature lyophilization, and chemical cross-linking, while maintaining the microstructure of the continuous nanofibers. The incorporation of short nanofibers led to a low release of melatonin and increased Young's modulus of the scaffold. Scaffold@MT demonstrated positive biocompatibility by promoting a 14.2 % increase in cell proliferation. In comparison to the control group, Scaffold@MT significantly enhanced matrix mineralization by 3.2-fold and upregulated the gene expression of osteoblast-specific markers, thereby facilitating osteogenic differentiation of bone marrow mesenchymal stem cells (BMMSCs). Significantly, Scaffold@MT led to a marked enhancement in the mitochondrial energy function of BMMSCs, evidenced by elevated adenosine triphosphate (ATP) production, mitochondrial membrane potential, and protein expression of respiratory chain factors. Furthermore, Scaffold@MT promoted the migration of human umbilical vein endothelial cells (HUVECs) and increased tube formation by 1.3 times compared to the control group, accompanied by an increase in vascular endothelial growth factor (VEGFA) expression. The results of *in vivo* experiments indicate that the implantation of Scaffold@MT significantly improved vascularized bone regeneration in a distal femur defect in rats. Micro-computed tomography analysis conducted 8 weeks post-surgery revealed that Scaffold@MT led to optimal development of new bone microarchitecture. Histological and immunohistochemical analyses demonstrated that Scaffold@MT facilitated bone matrix deposition and new blood vessel formation at the defect site. Overall, the utilization of melatonin-loaded nanofiber sponges exhibits significant promise as a scaffold that promotes bone growth and angiogenesis, making it a viable option for the repair of critical-sized bone defects.

* Corresponding author. Department of Orthopaedics, The First Affiliated Hospital of Soochow University, Soochow University, Suzhou, 215006, China.
** Corresponding author. Department of Pathology, The Third Affiliated Hospital of Soochow University, Changzhou, 213003, China.
*** Corresponding author. Department of Orthopaedics, The Affiliated Lianyungang Clinical College of Xuzhou Medical University, Lianyungang, 222003, China.
E-mail addresses: liqblk@163.com (Q. Li), drliumingming@163.com (M. Liu), fanhe@suda.edu.cn (F. He).
[1] Nanning Lv, Mingzhuang Hou, and Lei Deng contributed equally to this work.

https://doi.org/10.1016/j.mtbio.2024.101078
Received 2 March 2024; Received in revised form 25 April 2024; Accepted 1 May 2024
Available online 3 May 2024

1. Introduction

The prevalence of bone defects resulting from traffic accidents, trauma, congenital malformations, and iatrogenic causes is steadily rising, significantly impacting quality of life [1]. Additionally, the mortality rate among the elderly population is progressively increasing [2]. Currently, autologous and allograft bone grafts are the primary approaches employed to address substantial bone defects. Nevertheless, these methods possess certain drawbacks, such as limited availability, susceptibility to infection and complications, and the potential for immune rejection [3]. In recent years, bone tissue engineering has emerged as a promising avenue for the repair of bone defects. Functional materials are integrated in a cohesive manner to construct an intelligent platform, while the incorporation of suitable growth factors is employed to enhance or restore biological tissue, thereby facilitating the effective remediation of bone defects [4].

Electrospinning, a powerful and extensively employed manufacturing technique, has garnered significant interest in the field of tissue engineering due to its ability to fabricate fibrous networks ranging from micro-to nanometer scale, utilizing diverse biomaterials including synthetic polymers, collagen, silk fibronin, and composite materials [5]. Electrospun nanofibers possess the ability to replicate the composition and arrangement of the native extracellular matrix (ECM), thereby promoting cell adhesion and proliferation. This is primarily attributed to their interconnected porous structure, high surface-to-volume ratio, and favorable biocompatibility [6]. Presently, these two-dimensional (2D) nanofibers are employed as synthetic periosteum for the purpose of mending calvarial defects, typically in the form of membranes or meshes. To illustrate, Cui et al. successfully fabricated a coaxial electrospun nanofibrous mat, comprising a dexamethasone-loaded core layer and a deferoxamine-loaded shell layer. They showed that the utilization of a dual-drug programmed releasing membrane effectively enhanced the regeneration of critical-size calvarial bone by sequentially stimulating both osteogenesis and angiogenesis [7]. However, the treatment of femoral bone defects using electrospun nanofibers confined within two-dimensional membranes presents a significant challenge due to the absence of mechanical support and the inherently dense fibrous structure, which restricts the infiltration of cells and deposition of matrix within the nanofibrous structure [8].

In order to transform conventional 2D electrospun membranes into macroscopic three-dimensional (3D) structures, several approaches have been devised, including liquid and template-assisted electrospinning, as well as the utilization of a specially designed collector [9,10]. Si et al. have documented a technique for fabricating an ultralight 3D nanofibrous aerogel by combining electrospinning and freeze drying methodologies. This involves converting an electrospun nanofiber membrane into smaller fragments or individual nanofibers, dispersing them in freeze-dried liquid, and subsequently cross-linking them to produce stable nanofibrous sponges using freeze drying molding [11]. The 3D short nanofiber sponges have been shown high porosity, water absorption, and compression resilience, and demonstrated superiority over 2D nanofiber membranes in reparing diabetic full-thickness skin defects [12], therefore attracting growing interests for tissue engineering applications. However, the 3D nanofiber sponge-like scaffold alone is insufficient to induce bone regeneration and new blood vessel formation due to the complex environment of the bone defect site, so bioactive and osteoinductive factors are necessary to enhance the repair effect of these short nanofiber sponges.

Melatonin, a neurohormone predominantly secreted by the pineal gland, has been implicated in a range of physiological processes, encompassing circadian rhythms, immune responses, inflammation, and oxidative stress [13,14]. Notably, melatonin assumes a crucial function in maintaining the equilibrium of bone metabolism [15], as it not only facilitates osteoblast-driven bone formation but also inhibits osteoclast-mediated bone resorption [16]. Chen et al. conducted a study that revealed the ability of melatonin administration to effectively restore the impaired osteogenic differentiation of bone marrow-derived mesenchymal stem cells (BMMSCs) in osteoporosis and to preserve bone mass and micro-architecture in ovariectomized rats, indicating its potential as a treatment for bone diseases [17]. Previous research has also explored the integration of melatonin with electrospun polymer materials, specifically by loading melatonin into polycaprolactone (PCL) nanofibers and incorporating them with sodium alginate hydrogels. This biomimetic composite scaffold was shown to facilitate tendon injury repair by activating the antioxidant stress pathway [18]. Our laboratory previously developed a straightforward cryopreservation technique, which effectively incorporated melatonin into a silk fibroin (SF)/gelatin methacrylate (GelMA) scaffold. The sustained release of melatonin from the scaffold significantly facilitated the repair process of a full-thickness articular cartilage defect [19]. However, the regenerative potential of melatonin-loaded electrospun nanofibers, particularly when utilized in the form of 3D sponge-like scaffolds, remains unexplored.

It is worth noting that the advantageous impact of melatonin on bone formation is closely associated with the enhancement of mitochondrial function in osteoblasts, potentially achieved through the augmentation of mitochondrial respiratory complex I and IV activity [20]. During the process of osteogenic differentiation in human mesenchymal stem cells (MSCs), there has been an observed upregulation of mitochondrial biogenesis and bioenergetic function. This is evidenced by the notable increase in intracellular adenosine triphosphate (ATP) content, oxygen consumption rate, copy number of mitochondrial DNA, and respiratory enzyme subunits. These findings suggest a transition in energy production from glycolysis to oxidative phosphorylation in MSC-differentiated osteoblasts [21]. Wan et al. fabricated a collagen membrane that was cross-linked with high molecular weight polyacrylic acid (HPAA) to enhance the osteogenesis of MSCs. They discovered that the composite collagen membrane facilitated mitochondrial biogenesis in response to the heightened energy requirements for osteogenic differentiation [22]. Consequently, it is imperative to investigate the underlying mechanism involving mitochondrial energy metabolism in the context of melatonin-loaded nanofiber sponge for bone defect repair.

While the osteogenic effects of melatonin have been extensively studied, there remains a paucity of research on its effects into angiogenesis. Neovascularization networks play a crucial role in bone regeneration during the repair process. Following the implantation of biomaterials into bone defects, the initiation of early neovascularization provides nutrients and oxygen, facilitating the transportation of metabolic substances necessary for bone tissue regeneration [23]. Piedad et al. observed that the incorporation of melatonin into bone grafts could enhance the expression of vascular endothelial growth factor (VEGFA) [24], while Yildirimturk et al. reported analogous results in their study on the treatment of tibial bone defects in diabetic rats using melatonin [25]. Furthermore, research has demonstrated that melatonin enhances blood circulation in murine models of posterior limb ischemia by facilitating mesenchymal stem cell-mediated angiogenesis [26]. These studies collectively imply that melatonin may enhance tissue ischemia and stimulate angiogenesis, ultimately expediting bone regeneration.

This study aimed to develop a 3D scaffold composed of gelatin and poly-lactic-acid (PLA) electrospun nanofibers, loaded with melatonin, with the intention of enhancing bone healing. The hypothesis was that the melatonin-loaded nanofiber scaffold, possessing interconnected porous structure and desirable mechanical properties, would promote regenerative capabilities. To assess the osteogenic and angiogenic performance, *in vitro* experiments were conducted to evaluate cell viability, migration, matrix mineralization, and mitochondrial function. The effectiveness of the melatonin-loaded nanofiber scaffold in bone regeneration was investigated in a rat femoral bone defect model (Fig. 1).

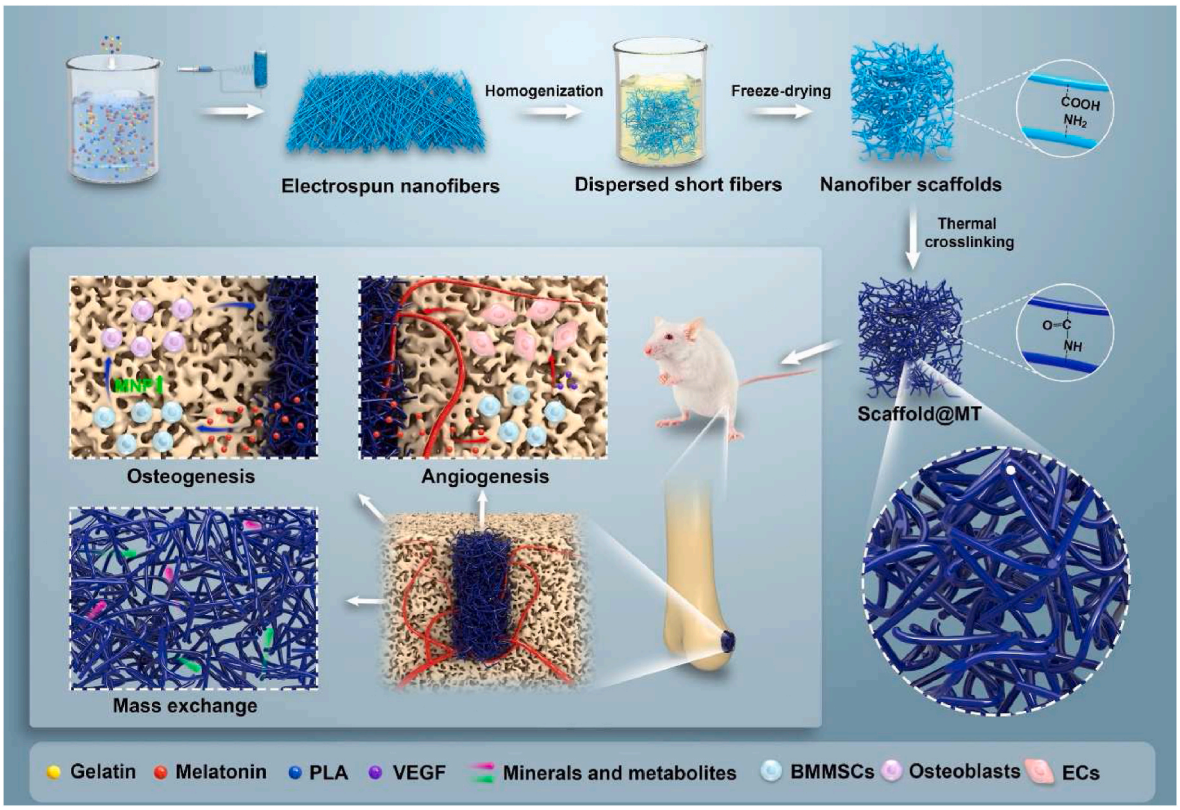

Fig. 1. Schematic diagram of the melatonin-loaded nanofiber scaffolds (Scaffold@MT) promoting vascularized bone regeneration.

2. Materials and methods

2.1. Fabrication of nanofiber sponge-like scaffolds

Initially, a solution comprising 4 g of gelatin and 1 g of oly-lactic-acid (PLA, 38534, Sigma-Aldrich, St. Louis, MO, USA) dissolved in 50 mL of 1,1,1,3,3,3-hexaffuoro-2-propanol (HFIP, 105228, Sigma-Aldrich) with a concentration of 10% w/v was prepared. The electrospinning process was conducted employing a voltage of 15 kV, a flow rate of 3 mL/h, and a collection distance of 15 cm. Specifically, the electrospun nanofiber was subjected to thorough drying in a dry and moderate environment to decrease its toughness, followed by crushing and cutting into pieces using a grinder. Subsequently, nanofiber membrane fragments were dispersed in tert-butanol (PHR2184, Sigma-Aldrich). Subsequently, the mixture underwent freeze-drying for 48 h, leading to the formation of uncross-linked scaffolds. To enhance the structural stability, the scaffolds were subsequently cross-linked in an oven maintained at a temperature of 150°C for 2 h.

In order to incorporate melatonin into EF-Scaffolds, a solution of 10 mL HFIP was utilized, containing 5 mg and 50 mg of melatonin (M5250, Sigma-Aldrich). The electrospinning technique was employed to fabricate nanofibers with varying dosages of melatonin. Consequently, Scaffold@LMT (representing 0.5% melatonin) and Scaffold@HMT (representing 5% melatonin) were successfully generated following the aforementioned procedures.

2.2. Characterization of EF-Scaffolds

The morphology of the EF membranes and EF-Scaffolds was examined through the utilization of a scanning electron microscope (SEM, S-4800, Hitachi, Kotyo, Japan). The average nanofiber diameter of both the EF membranes and EF-Scaffolds was determined by employing the Image J software (National Institutes of Health, Bethesda, MD, USA). Physicochemical characterization was carried out by means of Fourier-transform infrared spectroscopy (FTIR, Nicolet 6700, Thermo Scientific, USA), with measurements conducted within a wave number range of 500 to 4,000 cm^{-1}. The mechanical properties of the scaffolds were assessed using an Instron 5865 material testing machine (Instron, Norwood, MA, USA). Compression strain-stress curves of the scaffolds were obtained at a strain rate of 10 mm/min.

An experiment was conducted to evaluate the swelling characteristics of scaffolds through a water absorption test. Initially, the weight of the dry scaffolds was determined and recorded as W0. Subsequently, the scaffolds were immersed in deionized water and their weights were measured and documented (Wt) at intervals of 15, 30, 45, 60, and 120 min. The water absorption (WA) was then calculated as (Wt-W0)/W0 × 100%.

2.3. Release profile of melatonin from Scaffold@LMT and Scaffold@HMT

To assess the release of melatonin, Scaffold@LMT and Scaffold@HMT were incubated in 1 mL of phosphate buffered saline (PBS, HyClone, Logan, UT, USA) at 37°C. At specific time points (1, 3, 5, 7, 9, 11, 13, 17, 21, and 25 d), the supernatant was collected and the cumulative release profiles of melatonin were determined using a spectrophotometer at an absorbance of 280 nm (Shimadzu Co., LTD, Shanghai, China), following the standard curve of melatonin.

2.4. Isolation and cell culture of BMMSCs

BMMSCs were obtained from the bone marrow of eight-week-old Sprague-Dawley (SD) rats. Following euthanasia, the femurs and tibias of the rats were collected and the bone marrow was flushed out three times with alpha minimum essential medium (α-MEM, Thermo Fisher Scientific, Waltham, MA, USA). The extracted cells were then cultured in α-MEM supplemented with 10% fetal bovine serum (FBS, Thermo Fisher Scientific), 100 U/mL penicillin, and 100 μg/mL streptomycin at a

temperature of 37°C with 5% CO_2. The culture medium was refreshed every three days. Upon reaching 90% confluence, the cells were detached using 0.25% trypsin-EDTA (Thermo Fisher Scientific). Cells at passage two (P2) were utilized for subsequent experiments.

2.5. Live/dead cell staining assay

Cell viability was determined using a live/dead cell staining kit (C2015 M, Beyotime, Haimen, China). BMMSCs were seeded in 24-well plates at a density of 1×10^5 cells per well and treated with the leachate of different scaffolds, while treatment with PBS served as the control (CTRL) group. At the time points of 1, 3, and 5 d, the cells were stained with a live/dead cell staining kit for 30min at 37 °C. The stained cells were observed and captured using an automated fluorescence microscope (Zeiss, Oberkochen, Germany).

2.6. Cell proliferation assay

Cell proliferation was measured with the Cell Counting Kit 8 Kit (CCK-8, C0038, Beyotime). A total of 1×10^3 BMMSCs were seeded in a 96-well plate and incubated with the leachate of different scaffolds. At predetermined intervals (1, 3, 5, and 7 d), the cells were incubated in CCK-8 solution in the dark for 1 h at 37°C. The absorbance at 450 nm was measured by a PowerWave XS spectrophotometer (BioTek, Winooski, VT, USA).

2.7. Scratch wound assay

When the cell confluence reached 95%, scratch wound assays were conducted by creating a straight and gentle scraping using a sterile pipette tip. After washing, the cells were incubated in α-MEM containing 0.1% FBS medium and the leachate of different scaffolds. The wound images were captured at different time intervals (12 and 24 h) using an optical microscope (Zeiss).

2.8. Osteogenic differentiation

To induce osteogenic differentiation, BMMSCs were incubated in osteogenic differentiation medium containing the leachate of different scaffolds. The osteogenic medium consisted of Dulbecco's modified Eagle medium (DMEM) supplemented with 10% FBS, 10 mM β-glycerol phosphate, 100 nM dexamethasone, and 50 μg/mL L-ascorbic acid (Sigma-Aldrich). The medium was refreshed every three days.

2.9. Measurement of alkaline phosphatase (ALP) activity

After a 7-day osteogenic induction, the differentiated BMMSCs were fixed with 4% paraformaldehyde (Sigma-Aldrich) for 30 min and incubated in the ALP staining solution (MAK530, Sigma-Aldrich) for 30min. The stained cells were observed using an optical microscope (Zeiss). To quantify the ALP activity, a commercially available ALP assay kit (Sigma-Aldrich) was used according to the manufacturer's protocol. The absorbance was measured at 520 nm using a spectrophotometer (BioTek). The protein concentration was determined using a bicinchoninic (BCA) acid protein assay kit (P0012, Beyotime), and the ALP activity was normalized to the total protein content.

2.10. Measurement of matrix mineralization

Following a 21-day duration of osteogenic differentiation, the differentiated BMMSCs were fixed using a 4% paraformaldehyde solution. After rinsing with deionized water, the cells were incubated in a 2% Alizarin red s (ARS) staining solution (C0148S, Beyotime) at room temperature for 20 min. The stained cell layers were captured by an optical microscope (Zeiss). In order to perform quantitative analysis, a 5% perchloric acid solution (Sigma-Aldrich) was introduced to dissolve the calcium nodule, and the absorbance was measured at a wavelength of 420 nm using a spectrophotometer (BioTek).

2.11. Measurement of intracellular ATP production

BMMSCs were subjected to lysis using ATP lysis buffer (Beyotime) and the cell suspensions were subjected to centrifugation at 12,000 g for 5 min at 4°C. The supernatant was incubated with ATP detection working solution (S0026, Beyotime) according to the manufacture's instructions. Luminescence analysis was performed using a Centro LB 960 (Berthold Technologies, Germany). The relative ATP production was normalized by measuring the protein content of each sample using a BCA protein assay kit (Beyotime).

2.12. Measurement of mitochondrial membrane potential (MMP)

The change of MMP was measured using a Mitochondrial Membrane Potential Assay Kit with JC-1 (C2006, Beyotime). The cells were subjected to incubation with a 0.5 μM JC-1 working solution in the absence of light at 37°C for 30 min. The fluorescence images were captured with a microscope (Zeiss) and analyzed using the Image J software.

2.13. Immunofluorescence staining

BMMSCs were fixed with 4% paraformaldehyde and permeabilized using 0.1% Triton X-100 (Beyotime) in PBS containing 5% bovine Serum albumin (BSA). After overnight incubation with the primary antibody against Type I collagen A1 (COL1A1, 1:500, ABclonal, Wuhan, China) and Osteocalcin (OCN, 1:500, ABclonal) at 4°C, the cells were incubated with a fluorescein isothiocyanate-conjugated secondary antibody (1:500, ABclonal) at room temperature for 1 h. The nuclei were counterstained with 4′,6-diamidino-2-phe-nylindole (DAPI, Thermo Fisher Scientific). Fluorescence images were captured using a Zeiss Axiovert 40CFL microscope.

2.14. Angiogenic effect of the nanofiber scaffolds

BMMSCs were treated with the leachate of different scaffolds, and the resulting conditioned medium was collected after 7 d of osteogenic induction. Human umbilical vein endothelial cells (HUVECs, Procell Life Science & Technology Company, Wuhan, China) were seeded on Matrigel (BD Biosciences, San Jose, CA, USA) following the manufacturer's instructions and incubated in the conditioned medium for 8 h. The formation of endothelial tubes was observed using an optical microscope, and the length of the tubes was quantified using Image J software.

2.15. Western blot

Total protein was extracted using radioimmunoprecipitation assay (RIPA) buffer containing protease inhibitors (Beyotime). The protein concentration was determined via the employment of a BCA Protein Assay Kit (Beyotime). Equal quantities of protein samples were separated using 10% sodium dodecyl sulfate-polyacrylamide gel electrophoresis (SDS-PAGE) and subsequently transferred to nitrocellulose membranes (Beyotime). After blocking, the membranes were incubated with primary antibodies overnight at 4°C. The following day, the membranes were incubated with horseradish peroxidase (HRP) labeled secondary antibodies (1:10,000, Beyotime) for 1 h at room temperature. The resulting bands were visualized using SuperSignal West Pico Substrate (Thermo Fisher Scientific) and the ChemiDoc Touch Imaging System (Bio-Rad). The intensity of the bands was analyzed using Image J software. Details of the primary antibodies used in this study are provided in Supplementary Table 1.

2.16. Reverse transcription-quantitative polymerase chain reaction (RT-qPCR)

Total RNA was extracted using TRIzol® reagent (Thermo Fisher Scientific), and the concentration was quantified using a NanoDrop 2000 (Thermo Fisher Scientific). The extracted RNA was reverse-transcribed into complementary DNA (cDNA) using a RevertAid First Strand cDNA Synthesis Kit (Thermo Fisher Scientific). Real-time PCR was carried out using an iTapTM Universal SYBR® Green Supermix kit (Bio-Rad, Hercules, CA, USA) in a CFX96TM Real-Time PCR System (Bio-Rad). The transcript levels of the target genes were determined using the comparative Ct ($2^{-\Delta\Delta Ct}$) method, with *Gapdh* (glyceraldehyde-3-phosphate dehydrogenase) as an internal standard. The primer sequences for the target genes are presented in Supplementary Table 2.

2.17. Establishment of a femur bone defect model

A total of 24 SD rats (aged 8 weeks and weighing 300–330 g) were purchased from the Animal Center of Soochow University. Animal experiments were performed in accordance with protocols approved by the Ethics Committee of Soochow University (No. SUDA20230402A05). The rats were maintained under standard aseptic conditions, encompassing consistent levels of humidity (50–60%), temperature (22–24°C), and a light-dark cycle from 6 a.m. to 6 p.m. Following a period of acclimatization lasting 1 week, the rats were anesthetized using intraperitoneal injection of 3% sodium pentobarbital (Shanghai Merck Co., Ltd., Shanghai, China) at a dosage of 1.5 mL/kg body weight. After creating a 2-cm incision on the left femur and exposing the lateral femoral condyle, a transcortical bone defect of 3 mm in diameter and 2 mm in depth was induced using an electric drill. The rats were assigned in a random manner to four groups: the Defect group left untreated, the Scaffold group, the Scaffold@LMT group, and the Scaffold@HMT group. Postoperatively, penicillin at a dosage of 6000 units was administered once daily for three consecutive days.

2.18. Micro-computed tomography (Micro-CT) analysis

After 4 and 8 weeks post-surgery, the rats were euthanized, and their femora were collected for micro-CT evaluation. The analysis employed a micro-CT scanning system (SkyScan 1176, Bruker Corporation, Billerica, MA, USA) by setting the following parameters: a width of 18 μm, a voltage of 65 kV, and a current of 385 μA. The software programs NRecon v1.6 and CTAn v1.13.8.1 (Bruker) were utilized for 3D reconstruction. The region of interest (ROI) reconstruction area for the defect was a constant segment located at the distal femur. To assess the bone microstructure, bone mineral density (BMD, g/cm^3), bone volume ratio (BV/TV, %), and trabecular number (Tb.N, 1/mm) were analyzed using CT Analyzer software (Bruker).

2.19. Histological analysis

The femur specimens underwent fixation in 4% paraformaldehyde and decalcification in 10% ethylene diamine tetraacetic acid (EDTA, Sigma-Aldrich). The specimens were embedded in paraffin (Leica, Wetzlar, Germany) and cut into 5 μm-thick sections. For hematoxylin and eosin (H&E) staining, the sections were stained with hematoxylin for 3 min, followed by eosin solution for 1min (all from Jiancheng, Nanjing, China). For Masson's trichrome staining, the sections were stained with a solution containing hematoxylin and lichun red acid for 5min each (Solaibao Technology Co., Ltd, Beijing, China). Digital images were captured using a bright field microscope (Zeiss).

2.20. Immunohistochemical (IHC) staining

The sections were subjected to deparaffinization using xylene, hydration with graded ethanol, and treatment with 3% hydrogen peroxide (Sigma-Aldrich) to inhibit endogenous peroxidase. Then, the sections were incubated with 2 mg/mL of testicular hyaluronidase (Sigma-Aldrich) for 30 min at 37°C and blocked using 1.5% goat serum. Subsequently, the sections were incubated with specific primary antibodies overnight at 4°C, including anti-COL1A1 (1:500), anti-VEGFA (1:500), and anti-CD31 (1:300, ABclonal). The following day, the sections were incubated with biotinylated goat anti-rabbit secondary antibodies for 30 min. Signal amplification was achieved using the Vectastain Elite ABC kit. The staining process involved the use of a 3,3′-diaminobenzidine (DAB) solution (all from Vector Laboratories, Burlingame, CA, USA), and counterstaining of the nuclei was performed using hematoxylin. Images were captured using a bright field microscope and analyzed using the Image J software.

2.21. Statistical analysis

All data were expressed as mean ± standard error of means. Statistical analyses were performed using GraphPad Prism 9.2 software (GraphPad Software Inc., San Diego, CA, USA). Multiple group comparisons were conducted using One-way Analysis of Variance (ANOVA) followed by Tukey's post hoc test, while two-group comparisons were performed using Student's *t*-test. P values < 0.05 (*) or < 0.01 (**) were considered as statistically significant.

3. Results

3.1. The fabrication and characterization of electrospun nanofiber-based scaffolds

The fabrication process of nanofiber sponges can be categorized into four sequential steps: electrospinning, grinding homogenization, low temperature lyophilization, and high temperature crosslinking (Fig. 2A). Gelatin/PLA nanofibers were fabricate using an electrospinning apparatus and subsequently fragmented into smaller pieces. These fragments were then immersed in tert-butanol to attain a homogeneous dispersion within the solution. The dispersions were subsequently subjected to freeze-drying and further enhanced through thermal crosslinking to construct sponge-like scaffolds. In order to assess the impact of nanofiber density on the structural and mechanical characteristics of the scaffolds, various fiber densities (1, 2, and 3%) were selected for the fabrication of the sponges. Analysis of the SEM results indicated that the nanofibers within the scaffolds exhibited a random arrangement (Fig. 2B). The average diameter of the nanofibers was measured at 990 nm, with a range spanning from 500 to 1,300 nm (Fig. 2C); however, no statistically significant differences were observed among the various scaffolds. Furthermore, it was observed that an increase in fragment concentration led to a progressive reduction in the size of the fiber pores within the scaffold. The unbound acidic groups and alkaline residues present in gelatin can be consolidated through the formation of intermolecular crosslinks and amide bonds during thermal cross-linking.

Analysis using FTIR demonstrated a notable increase in the absorption intensity peak (1,643 cm^{-1}) associated with the C–N stretching vibration band in the spectra of nanofiber scaffolds (Fig. 2D). Furthermore, our findings indicate a significant enhancement in the water absorption capacity of nanofiber scaffolds compared to the EF group (Fig. 2E). This observed increase in water absorption can be primarily attributed to the heightened porosity of the scaffolds, particularly the reduced density of fractured fibers. The compressive strength of scaffolds composed of varying concentrations of EF is presented in Fig. 2F. As the concentration of fragments increased, the compression modulus of the scaffolds exhibited a gradual increase. Notably, the Young's modulus of the 3% EF Scaffold group (0.294 kPa) was significantly higher compared to the 1 % EF Scaffold (0.103 kPa) and 2% EF Scaffold (0.190 kPa) groups. Taking into account the favorable water absorption, porosity, and mechanical properties observed in the 2% EF Scaffold, it was chosen as the suitable candidate for melatonin loading. Fig. 2G

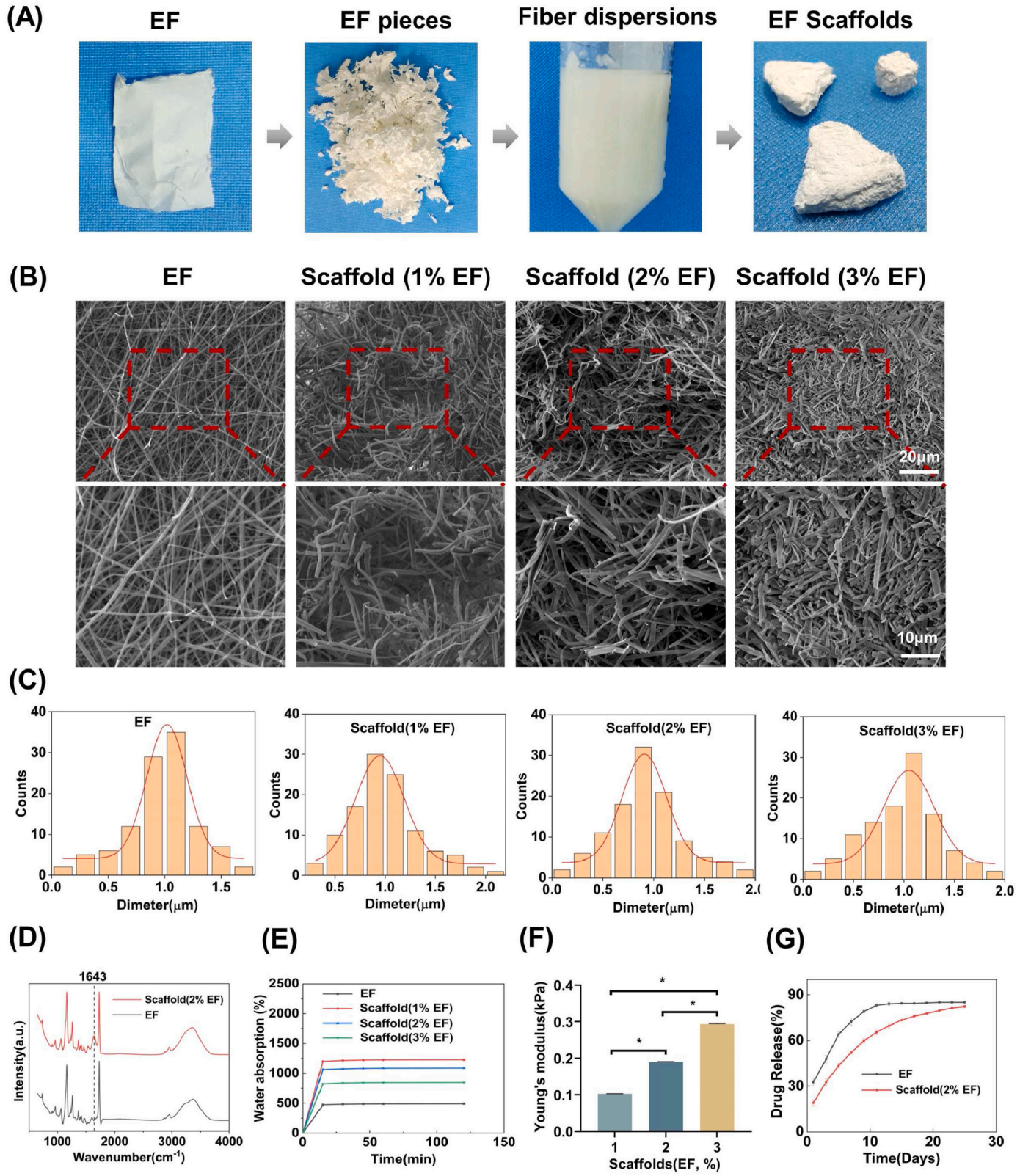

Fig. 2. Morphology and characterization of electrospun fiber scaffolds (EF-Scaffold). (A) The preparation process of EF Scaffolds included electrospinning, grinding homogenization, low temperature lyophilization, and high temperature crosslinking. (B) Representative SEM images of EF membranes and EF Scaffolds. (C) Fiber diameter distributions of EF membranes and EF Scaffolds. (D) FTIR spectra of EF membranes and Scaffold (2 % EF). (E) Water absorption of EF membranes and EF Scaffolds. (F) Compressive mechanical properties of Scaffolds that contained 1 %, 2 %, or 3 % electrospun nanofibers. (G) Release profile of melatonin from EF membranes and Scaffold (2 % EF).

demonstrated the *in vitro* release of melatonin from the EF membranes and 2 % EF Scaffold. The release profile analysis of the 2% EF Scaffold reveals an initial rapid release of melatonin within the first 3 days (32.7%), followed by a slower release until day 21 (79.7%).

3.2. Biocompatibility of melatonin-loaded nanofiber scaffolds

To investigate the impact of nanofiber scaffolds loaded with melatonin on cell viability and proliferation, BMMSCs were exposed to Scaffold, Scaffold@LMT, and Scaffold@HMT-extracted leachate. Live/dead cell staining reveals a significant number of viable cells with minimal presence of deceased cells, suggesting that the nanofiber scaffolds exhibited favorable biocompatibility (Fig. 3A-B). The CCK-8 assays demonstrated that the cell proliferation of BMMSCs was significantly enhanced by Scaffold@HMT, with a 14.2% and 5.5% increase compared to the Scaffold and Scaffold@LMT groups, respectively, on day 5 (Fig. 3C). Furthermore, the scratch assay revealed that the Scaffold@LMT and Scaffold@HMT groups exhibited significantly larger

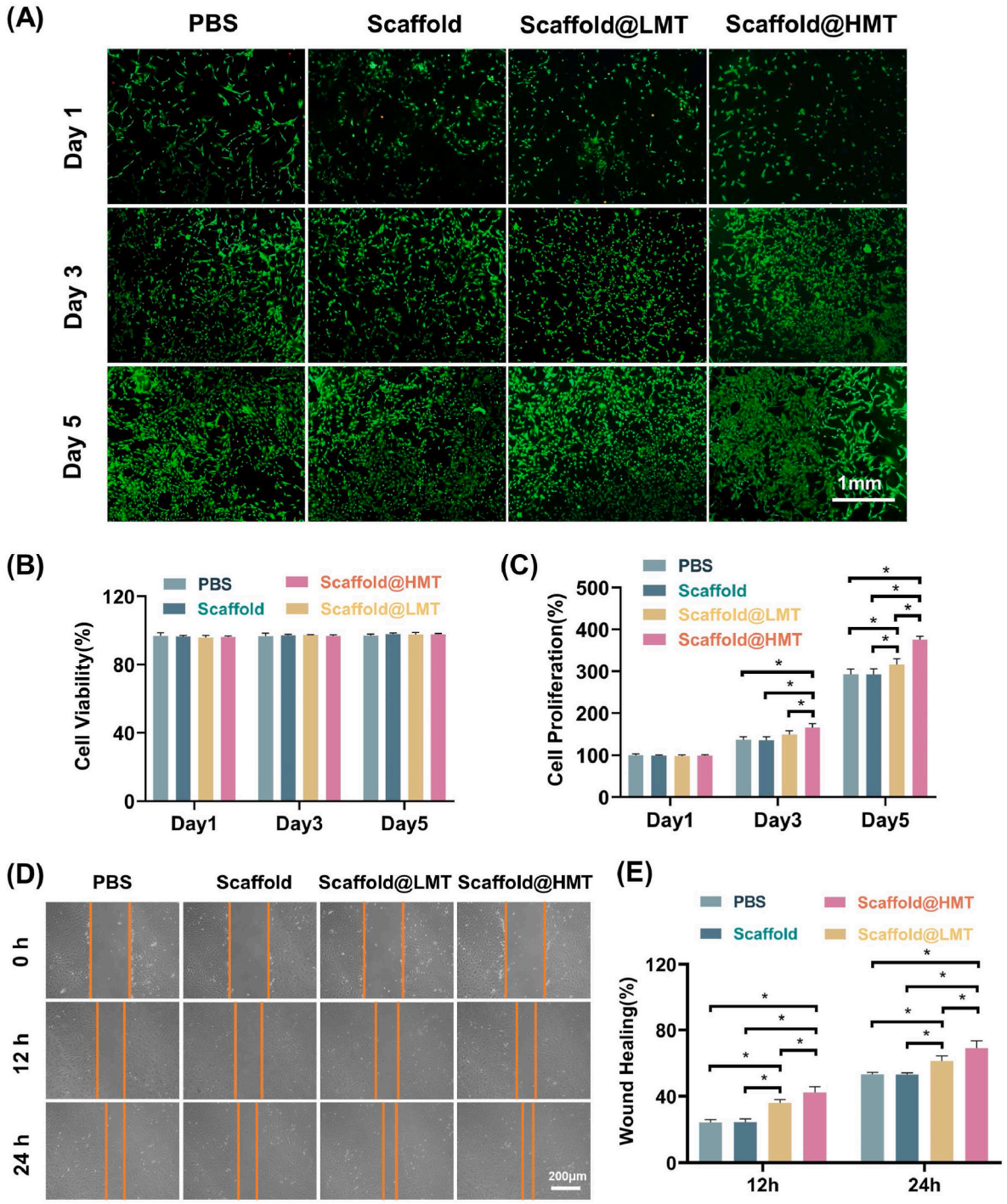

Fig. 3. Biocompatibility of melatonin-loaded nanofiber scaffolds. Bone marrow mesenchymal stem cells (BMMSCs) were exposed to Scaffold, Scaffold@LMT, or Scaffold@HMT-extracted leachate, while cells treated with phosphate-buffered saline (PBS) served as the control (CTRL) group. (A-B) Cell viability was compared by a live/death staining assay, n = 3. Scale bar: 1 mm. (C) Cell proliferation was examined on Days 1, 3, and 5 using CCK-8 assay, n = 5. (D-E) Cell migration capacity of BMMSCs was determined by a scratch assay. n = 3. Data are presented as means ± SEM. Statistically significant differences were indicated by * $P < 0.05$.

healing areas at 12 and 24 h compared to the Scaffold group (Fig. 3D). Specifically, Scaffold@HMT significantly enhanced the migration capacity of BMMSCs by 73.5% (12 h) and 29.6% (24 h) compared to the Scaffold group (Fig. 3E).

3.3. Melatonin-loaded nanofiber scaffolds promoted the osteogenic differentiation of BMMSCs

The subsequent assessment involved evaluating the impact of melatonin-loaded nanofiber scaffolds on the osteogenic potential of BMMSCs. As an early marker of differentiation, the Scaffold@HMT group exhibited a more pronounced staining of ALP, indicating a higher proportion of differentiated BMMSCs (Fig. 4A). Quantitative analysis revealed that the ALP activity in the Scaffold@HMT group was significantly greater than that in the Scaffold and Scaffold@LMT groups, with increases of 2.1-fold and 53.2%, respectively (Fig. 4B). Calcium nodules are an indicator of late osteogenic differentiation. Following a 21-day period of osteogenic induction, a substantial number of calcium nodules, positively stained with Alizarin Red S, were observed in the Scaffold@LMT and Scaffold@HMT groups (Fig. 4C). The findings from the quantitative analysis demonstrated that the matrix mineralization in the Scaffold@HMT group was 3.2- and 1.2-fold greater than that of the Scaffold and Scaffold@LMT groups, respectively (Fig. 4D).

Furthermore, the expression levels of osteogenic markers, namely *Col1a1*, *Runx2*, and *Sp7*, were significantly up-regulated in BMMSCs cultured in both the Scaffold@LMT and Scaffold@HMT groups (Fig. 4E). Specifically, the mRNA expression of *Col1a1* in the Scaffold@LMT and Scaffold@HMT groups exhibited a significant increase of 82.2% and 1.4-fold, respectively, compared to the Scaffold group. The mRNA expression of *Runx2* and *Sp7* in the Scaffold@HMT group was significantly higher by 1.8-fold and 85.6 %, respectively, in comparison to the Scaffold group. The RT-qPCR results were further validated through Western blot analysis, which revealed a corresponding increase in protein levels of osteogenic markers in both the Scaffold@LMT and Scaffold@HMT groups (Fig. 4F). Notably, the Scaffold@HMT group exhibited the highest levels of COL1A1, RUNX2, and SP7 among all groups, with a significant increase of 1.0-fold, 88.9%, and 63.6%, respectively, compared to the Scaffold group (Fig. 4G). Immunofluorescence staining further confirmed the strong positive staining for COL1A1 in the Scaffold@LMT and Scaffold@HMT groups (Fig. 4H&I). Moreover, the nanofiber scaffold containing melatonin notably enhanced the expression of OCN (Supplementary Fig. 1A), while the Scaffold@HMT group demonstrated the highest OCN fluorescence intensity compared to all other groups (Supplementary Fig. 1B). These findings provide evidence that the Scaffold@HMT effectively enhances the osteogenic differentiation of BMMSCs, as indicated by higher levels of matrix mineralization and osteogenic-specific marker expression.

3.4. Melatonin-loaded nanofiber scaffolds improved the mitochondrial energy metabolism of BMMSCs

Given the importance of mitochondrial function in bone repair through its role in providing energy for matrix synthesis and calcium deposition, our study aimed to investigate the impact of melatonin-loaded nanofiber scaffolds on the mitochondrial energy metabolism of BMMSCs. To assess the depolarization of mitochondria in BMMSCs, we utilized JC-1 staining (Fig. 5A). The levels of MMP in the groups treated with Scaffold@LMT and Scaffold@HMT were found to be significantly higher, with a 1.3-fold and 2.0-fold increase, respectively, compared to the Scaffold group (Fig. 5B). Furthermore, treatment with Scaffold@LMT and Scaffold@HMT resulted in a significant increase in ATP production, with a respective increase of 29.1% and 59.9% compared to the Scaffold group (Fig. 5C). Moreover, the administration of melatonin-loaded nanofiber scaffolds resulted in a significant up-regulation of transcript levels associated with mitochondrial respiratory chain factors. Specifically, the expression of the *Atp5a* gene was increased by 87.2% in BMMSCs in the Scaffold@HMT group compared to the Scaffold group. Similarly, the expression of *Nd4* was increased by 1.0-fold and *Sdha* by 1.4-fold in the Scaffold@HMT group compared to the Scaffold group (Fig. 5D). Western blot analyses further confirmed the effectiveness of the Scaffold@LMT and Scaffold@HMT groups in improving the protein levels of ATP5A, ND4, and SDHA (Fig. 5E). Notably, the protein expression of ATP5A was increased by 90.5%, ND4 by 1.2-fold, and SDHA by 80.4% in the Scaffold@HMT group compared to the Scaffold group (Fig. 5F). The Scaffold@HMT group significantly enhanced the expression of COX4 and UQCRC1 proteins, with levels 0.6- and 2.7-fold higher than those observed in the Scaffold group, respectively (Supplementary Fig. 2). These data demonstrated that the utilization of melatonin-loaded nanofiber scaffolds resulted in enhanced energy production and improved mitochondrial function of BMMSCs.

3.5. Melatonin-loaded nanofiber scaffolds regulated the angiogenesis

To further investigate the potential impact of melatonin-loaded nanofiber scaffolds on angiogenesis, HUVECs were exposed to the conditioned medium derived from differentiated BMMSCs cultured in different scaffold groups. The scratch wound assay revealed a significant increase in the migration capacity of HUVECs in the Scaffold@LMT and Scaffold@HMT groups (Fig. 6A). Specifically, after 24 h of scratch, the healing area of the Scaffold@LMT and Scaffold@HMT groups was found to be 14.0% and 29.2% higher, respectively, compared to the Scaffold group (Fig. 6B). Moreover, a tube formation assay was conducted to assess the impact of scaffolds on angiogenic capacity. The results indicated a significantly higher number of endothelial tubes in the Scaffold@HMT groups compared to the other three groups (Fig. 6C). Quantitative analysis demonstrated that the tube length in the Scaffold@HMT group was 1.3-fold, 1.4-fold, and 54.2%, respectively, greater than the PBS, Scaffold, and Scaffold@LMT groups (Fig. 6D). Additionally, immunofluorescence staining revealed a significant elevation in CD31 expression in the Scaffold@HMT group compared to the PBS, Scaffold, and Scaffold@LMT groups, with respective increases of 3.2-fold, 3.1-fold, and 84.5% (Fig. 6E&F). The results obtained from RT-qPCR and Western blot assays confirmed that the group treated with Scaffold@HMT exhibited the highest level of VEGFA expression at both mRNA and protein levels. Specifically, the treatment with Scaffold@HMT resulted in a 1.1-fold up-regulation of *Vegfa* gene expression (Fig. 6G) and a 92.4% increase in VEGFA protein levels (Fig. 6H&I) compared to the group treated with PBS. Immunofluorescence staining for VEGFA also showed a similar trend, with Scaffold@HMT treatment significantly enhancing VEGFA expression (Fig. 6J&K). These findings suggest that the use of melatonin-loaded nanofiber scaffolds effectively enhances the expression of VEGFA in HUVECs, thereby promoting the formation of endothelial tubes.

3.6. Melatonin-loaded nanofiber scaffolds promoted vascularized bone regeneration

To assess the therapeutic efficacy of the melatonin-loaded nanofiber scaffolds, critical-sized femur bone defects were induced in SD rat femurs, followed by the implantation of scaffolds into the defects. Micro-CT scans were conducted at 4 and 8 weeks post-surgery to assess bone repair. The 3D reconstruction images revealed that, in comparison to the inadequate healing observed in the Defect group, the implantation of Scaffold@LMT and Scaffold@HMT effectively repaired the femur bone defects, as evidenced by the presence of new bone formation along the defect edges (Fig. 7A). Quantitative analysis demonstrated that the implantation of Scaffold@HMT resulted in the attainment of optimal efficiency in the development of new bone microarchitecture. Specifically, the implantation of Scaffold@HMT yielded a significant increase in BMD (Fig. 7D), with values 21.3 % higher at 4 weeks post-surgery and 27.9% higher at 8 weeks post-surgery compared to the Defect group. Furthermore, at 8 weeks post-surgery, the Scaffold@HMT group exhibited Tb.N

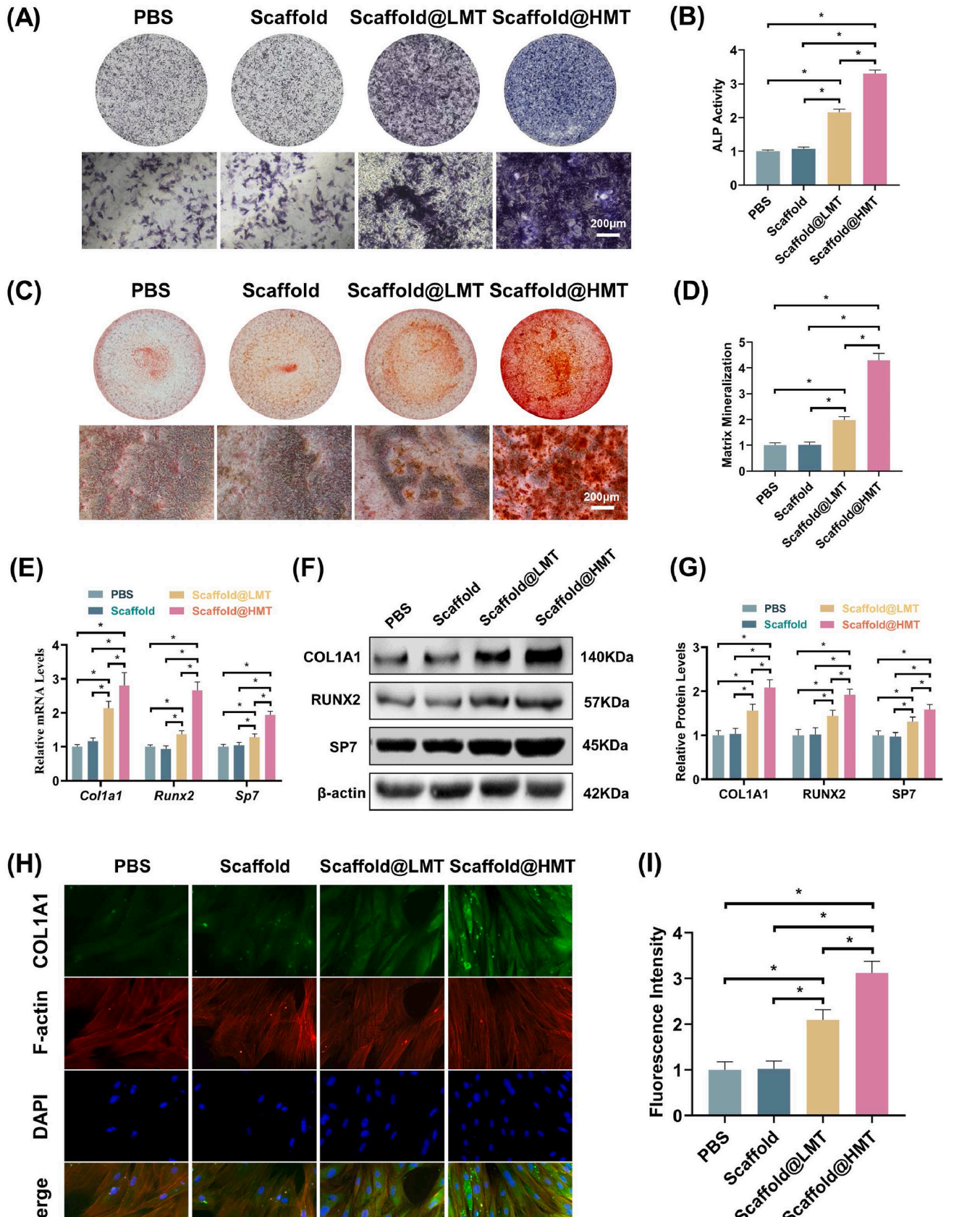

(caption on next page)

Fig. 4. Effect of melatonin-loaded nanofiber scaffolds on the osteogenic differentiation of BMMSCs. Bone marrow mesenchymal stem cells (BMMSCs) were induced toward the osteogenic differentiation and treated with Scaffold, Scaffold@LMT, or Scaffold@HMT-extracted leachate. Cells treated with phosphate-buffered saline (PBS) served as the control (CTRL) group. (A) ALP staining was performed after 7 days of induction. Scale bar = 200 μm. (B) Quantitative analysis of ALP activity, n = 4. (C) Alizarin Red S (ARS) staining was performed after 21 days of induction. Scale bar = 200 μm. (D) Quantification of the stained mineral layers indicated matrix mineralization, n = 4. (E) The gene expression of osteogenic makers, including *Col1a1*, *Runx2*, and *Sp7*, was determined by RT-PCR, n = 4. (F-G) The protein levels of COL1A1, RUNX2, and SP7 were examined by Western blot. n = 3. (H) Immunofluorescence staining of COL1A1 in differentiated BMMSCs. Scale bar = 50 μm. (I) Quantitative analysis of fluorescence intensity of COL1A1, n = 3. Data are presented as means ± SEM. Statistically significant differences were indicated by * $P < 0.05$.

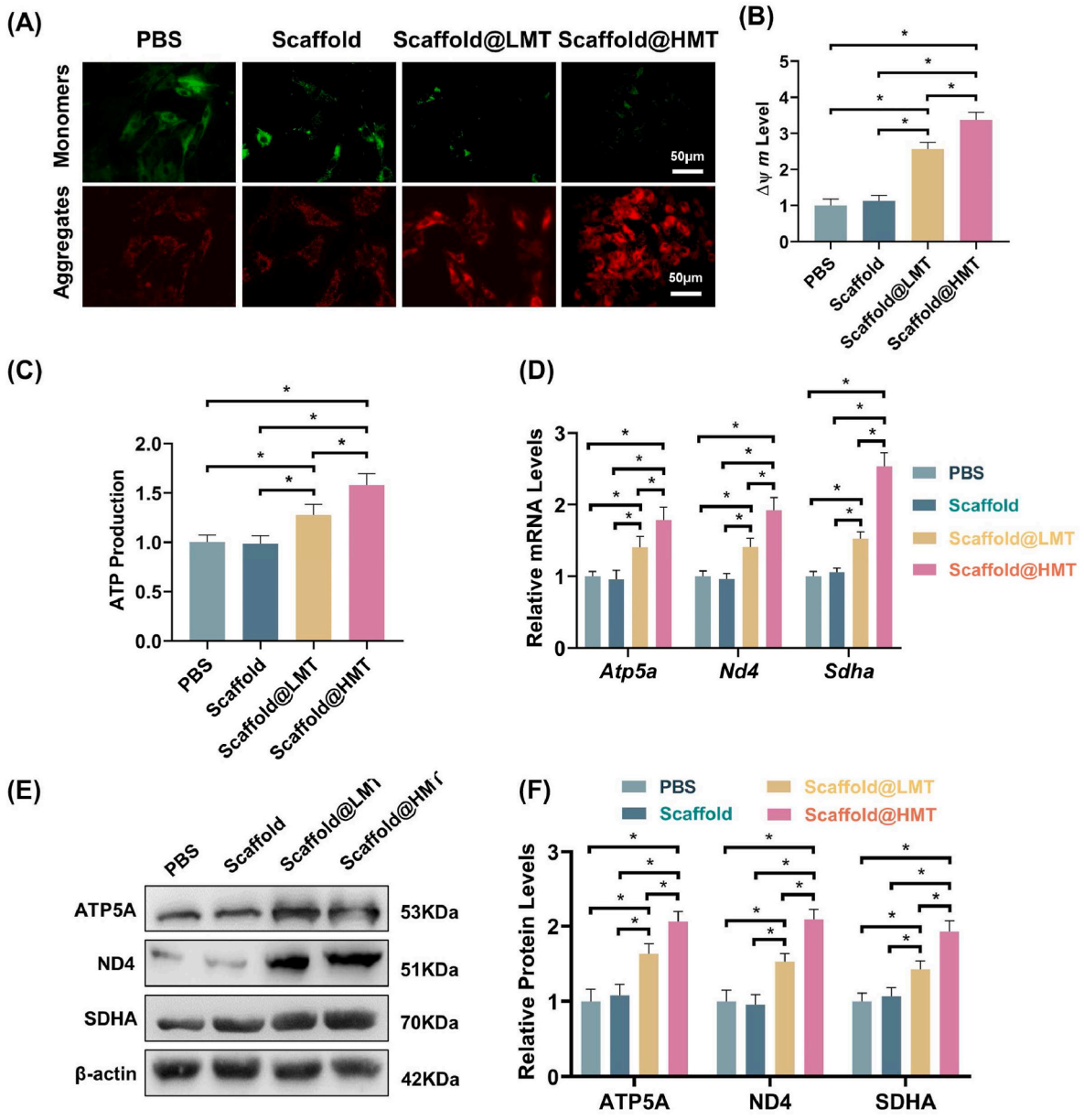

Fig. 5. Melatonin-loaded nanofiber scaffolds improved the mitochondrial energy metabolism of BMMSCs. (A) Immunofluorescence staining of JC-1 indicated mitochondrial membrane potential (MMP) levels. Scale bar = 50 μm. (B) Quantitative analysis of JC-1 fluorescence intensity, n = 3. (C) The effect of melatonin-loaded nanofiber scaffolds on ATP production, n = 3. (D) The gene expressions of mitochondrial respiratory chain factors (*Atp5a*, *Nd4*, and *Sdha*) were quantified with RT-qPCR, n = 4. (E-F) The protein levels of ATP5A, ND4, and SDHA were determined using Western blot, n = 3. Data are presented as means ± SEM. Statistically significant differences were indicated by * $P < 0.05$.

(Fig. 7C) and BV/TV (Fig. 7B) values that were 59.9% and 58.8% higher, respectively, than those observed in the Defect group.

In order to further investigate the formation of new bone in the areas affected by defects, histological analysis of femur samples was conducted. The results of H&E staining showed that, at 4 and 8 weeks post-surgery, only connective tissue was observed in the Defect and Scaffold groups. In contrast, the implantation of Scaffold@LMT and Scaffold@HMT resulted in a significant regeneration of bone tissues, as evidenced by the presence of calcium nodule deposition at the site of the defect (Fig. 8A). Furthermore, Masson's trichrome staining demonstrated a considerable amount of positive collagen staining in the Scaffold@HMT group at 4 and 8 weeks post-surgery, indicating that

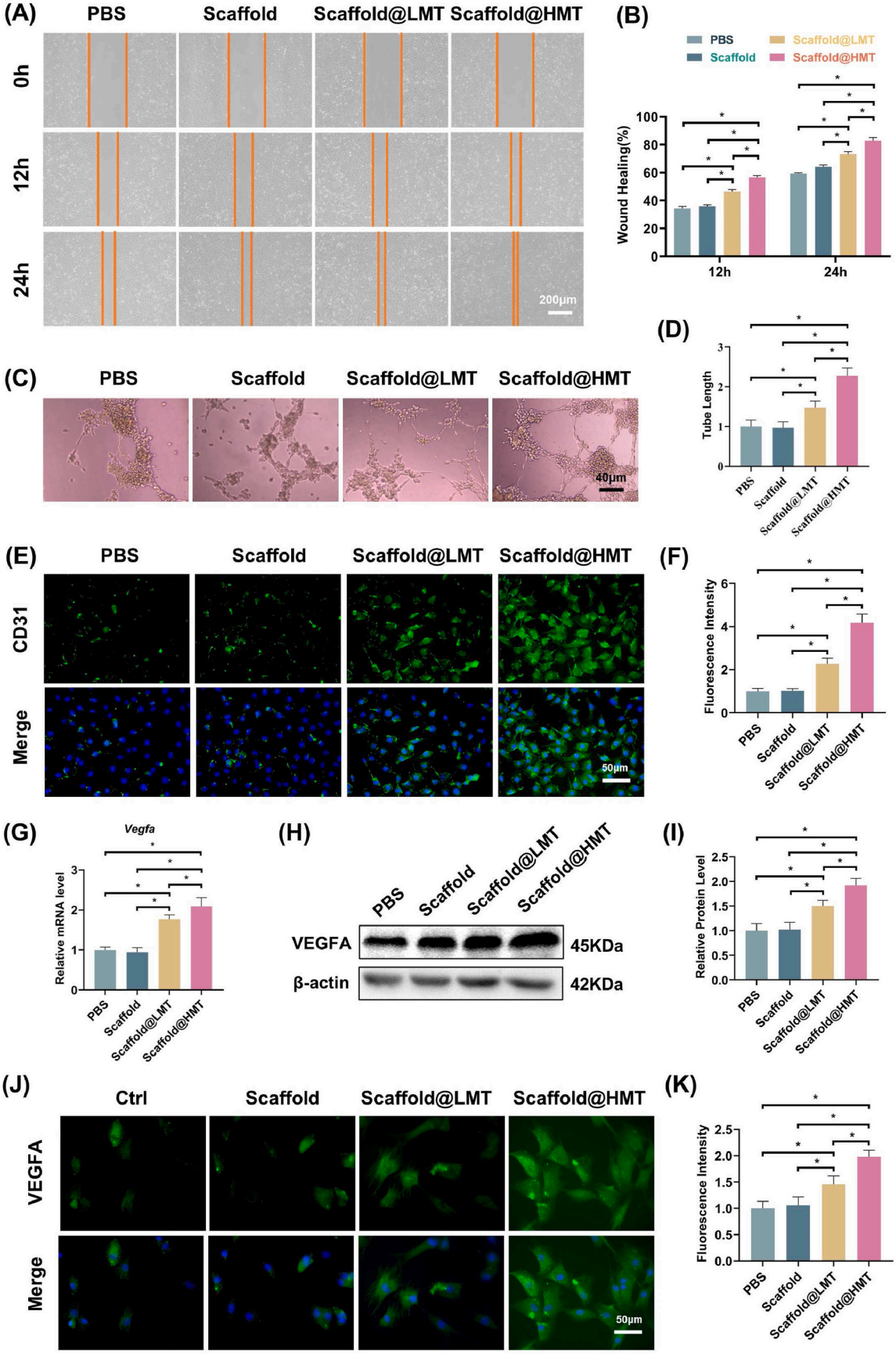

(caption on next page)

Fig. 6. Melatonin-loaded nanofiber scaffolds promoted the angiogenesis of endothelial cells. Human umbilical vein endothelial cells (HUVECs) were treated with the conditioned medium derived from differentiated BMMSCs on the different scaffold groups(A-F). Bone marrow mesenchymal stem cells (BMMSCs) were treated with Scaffold, Scaffold@LMT, or Scaffold@HMT-extracted leachate(G-K). (A) Cell scratch assay of HUVECs at 0, 12, and 24 h. Scale bar = 200 μm. (B) Quantitative analysis of cell scratch assay, n = 3. (C) Representative images of endothelial tube formation. Scale bar = 40 μm. (D) Quantitative analysis of endothelial tube length, n = 3. (E) Immunofluorescence staining of CD31 in HUVECs. Green: CD31, blue: DAPI. Scale bar = 50 μm. (F) Quantitative analysis of CD31 fluorescence intensity, n = 3. (G) The gene expression of *Vegfa*, n = 4. (H-I) The protein levels of VEGFA, n = 3. (J) Immunofluorescence staining of VEGFA in BMMSCs. Green: VEGFA, blue: DAPI. (K) Quantitative analysis of fluorescence intensity of VEGFA, n = 3. Data are presented as means ± SEM. Statistically significant differences were indicated by * $P < 0.05$.

Scaffold@HMT facilitated the formation of bone matrix and thus expedited the process of bone healing (Fig. 8B).

Immunohistochemical staining revealed a strong positive staining for COL1A1 in the Scaffold@HMT group, which was consistent with the results obtained from H&E staining, thus suggesting the synthesis of new bone matrix at the site of the defect (Fig. 9A). Quantitative analysis further demonstrated that the expression level of COL1A1 in the Scaffold@HMT group was 1.2-fold higher at 4 weeks post-surgery and 1.4-fold higher at 8 weeks post-surgery compared to the Defect group (Fig. 9B). In order to investigate the impact of Scaffold@HMT on angiogenesis, immunohistochemical staining was performed to assess the presence of VEGFA (Fig. 9C) and CD31 (Fig. 9E). Following the implantation of Scaffold@HMT, the quantity of VEGFA-positive cells exhibited a 1.9-fold increase at 4 weeks post-surgery and a 1.2-fold increase at 8 weeks post-surgery, surpassing the count observed in the Defect group (Fig. 9D). Additionally, the proportion of CD31-positive cells experienced a 1.4-fold increase at 4 weeks post-surgery and a 1.0-fold increase at 8 weeks post-surgery, in comparison to the Defect group (Fig. 9F). These findings serve to demonstrate the efficacy of Scaffold@HMT in augmenting bone regeneration and facilitating neovascularization, thereby promoting the mending of bone defects.

4. Discussion

In the field of bone tissue engineering, electrospinning has emerged as a subject of significant interest due to its ability to create a structure that mimics the ECM while also offering a high surface-to-volume ratio. Electrospun nanofibers have been shown to influence cell proliferation and osteogenic differentiation of BMMSCs due to their large specific surface area and high porosity [27,28]. In addition, electrospun nanofibers have demonstrated the potential for localized and controllable drug delivery, thanks to their user-friendly nature and adaptability. Given their distinctive membrane-like structure and appropriate physicochemical properties, electrospun fibers are predominantly employed as dressings for wound healing purposes. Nezamoleslami et al. Designed a sandwich-structured multilayered mat and demonstrated that the release of ceftazidime from the internal gelatin layer could be controlled, resulting in a significant antibacterial effect while having minimal impact on fibroblast cell viability [29]. In a similar vein, Mao et al. developed a multilayer electrospun nanofibrous membrane to facilitate bone regeneration. Their findings revealed that the sequential release of MT01 (a single-stranded cytosine–phosphate–guanosine oligodeoxynucleotide) from the inner layer and stromal cell-derived factor 1α (SDF-1α) from the outer layer effectively stimulated the recruitment of stem cells during the early phase and promoted osteogenic differentiation during the late phase, thereby promoting bone regeneration in a rat calvarial bone defect model [30]. Nevertheless, the utilization of electrospun nanofibers in tissue engineering is hindered by their relatively low porosity and weak mechanical strength. In order to address this limitation, the technique of freeze-drying dispersions of short electrospun fibers has been devised as a straightforward approach to fabricate ultraporous sponges possessing remarkable reversible compressibility, which is contingent upon the concentration of the fiber dispersion [31]. In an effort to identify the most suitable bio-elastomers for hemostatic dressings, Guo et al. successfully fabricated a three-dimensional loose sponge composed of interconnected polyurethane nanofibers and gelatin hydrogel. They demonstrated that the composite sponge's notable water absorption ratio facilitated prompt hemostasis in a rat liver injury model [32]. Within this investigation, a three-dimensional sponge-like scaffold loaded with melatonin was created through electrospinning, freeze-drying, and high temperature cross-linking techniques. To the best of our knowledge, this is the initial report on the successful implementation of this nanofiber sponge for the effective restoration of critical-sized femoral bone defects in rats.

In the context of bone regeneration, both the proliferation of BMMSCs and the synthesis of bone matrix by osteoblasts necessitate a consistently and intensively active mitochondrial metabolism to fulfill their energy demands [33]. In an effort to address diabetic bone fractures, Chen et al. devised an energy-regulating artificial periosteum by incorporating electrospun GelMA nanofibers and deferoxamine. This biomimetic electrospun membrane effectively enhanced the healing process of bone fractures by augmenting the mitochondrial respiration of BMMSCs [34]. In a recent study conducted in our laboratory, it was found that the utilization of selenium-modified calcium phosphate cement resulted in the restoration of mitochondrial function in BMMSCs. This was achieved by upregulating the antioxidant enzyme glutathione peroxidase 1 (GPX1), leading to effective repair of femoral bone defects in an ovariotomy-induced osteoporosis rat model [35]. Building upon these findings, the present study aimed to develop a nanofiber scaffold loaded with melatonin in order to enhance various cellular processes including proliferation, differentiation, matrix mineralization, and mitochondrial function of BMMSCs. It was observed that melatonin supplementation improved mitochondrial metabolism and mitigated oxidative stress within the mitochondria, potentially through the activation of the 5′ adenosine monophosphate-activated protein kinase (AMPK)/peroxisome proliferator-activated receptor-gamma coactivator 1 alpha (PGC1α) pathway [36]. Jiang et al. have successfully fabricated a composite scaffold composed of polycaprolactone and graphene oxide, which is loaded with melatonin in multiple layers. This scaffold exhibits remarkable mechanical properties, including a high elastic modulus and structural integrity, and the controlled release of melatonin from the scaffold leads to an increase in ATP production, thereby promoting nerve regeneration. This is evidenced by the observed stimulation of myelination and axonal outgrowth, as well as a reduction in Schwann cell apoptosis [37]. Consequently, the melatonin-mediated enhancement of mitochondrial function provides an ample energy supply for the formation of bone matrix and the deposition of calcium.

The study found that after 7 days of osteogenic induction, the ALP activity in the Scaffold@LMT and Scaffold@HMT groups was notably higher compared to the PBS and Scaffold groups, suggesting that the melatonin-loaded nanofiber scaffold facilitated early osteogenic differentiation of BMMSCs. Alizarin red staining was utilized as a conventional technique to evaluate calcium nodules [38]. After 21 days of osteogenic induction, the Scaffold@HMT group exhibited the most intense staining of calcium nodules, suggesting its potential for matrix calcification. Immunofluorescence staining revealed that Scaffold@HMT significantly enhanced the expression of OCN, potentially attributable to melatonin release from the nanofiber scaffolds. Furthermore, melatonin consistently facilitated the differentiation of MC3T3-E1 cells into osteoblasts by upregulating OCN expression levels [39].

Despite the extensive evidence demonstrating the positive effects of melatonin on osteogenesis, its impact on angiogenesis remains a topic of debate. Research has shown that melatonin significantly suppresses cell

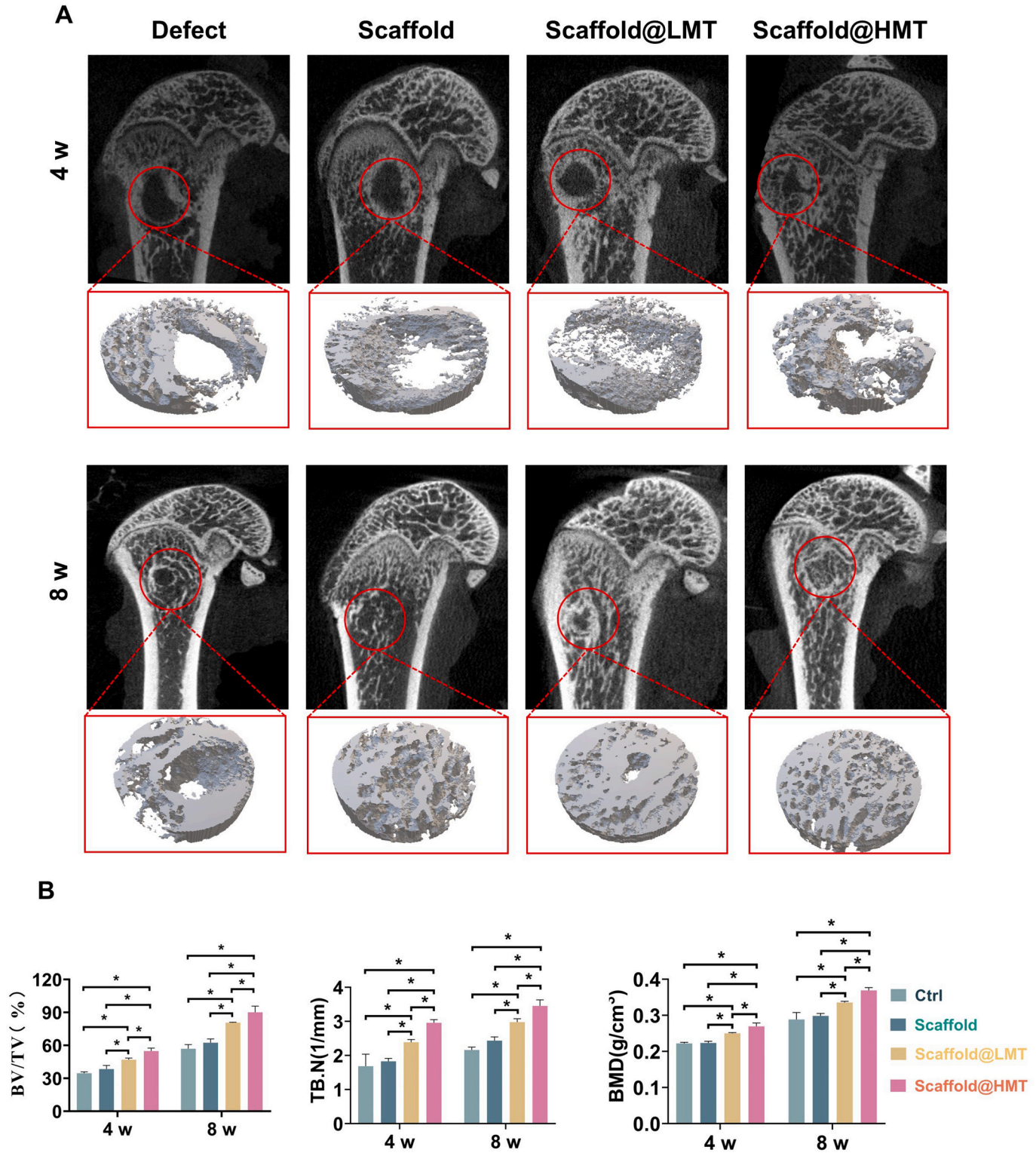

Fig. 7. Micro-CT evaluation of *in vivo* bone defect regeneration. Bone defects of 3 mm in diameter and 2 mm in depth were established in SD rat femur and melatonin-loaded scaffolds were implanted into the defects. (A) The new bone formation in the bone defects evaluated by micro-CT imaging and 3D reconstruction at 4 and 8 w. (B-D) Quantitative analysis of BV/TV, TB.N, and BMD in defect area, n = 3. Data are presented as means ± SEM. Statistically significant differences were indicated by * $P < 0.05$ or ** $P < 0.01$.

proliferation, migration, and tube formation in HUVECs by down-regulating the expression of VEGF [40]. Consequently, melatonin is being recognized as an effective antiangiogenic agent that can impede tumor growth and progression [41–43]. Furthermore, the intraperitoneal administration of melatonin demonstrated significant efficacy in mitigating the progression of post-traumatic osteoarthritis and improving the degradation of articular cartilage through the inhibition of vascular endothelium proliferation and synovial angiogenesis [44]. While melatonin did not directly promote angiogenesis, its antioxidant properties were found to positively impact the functional integrity of the

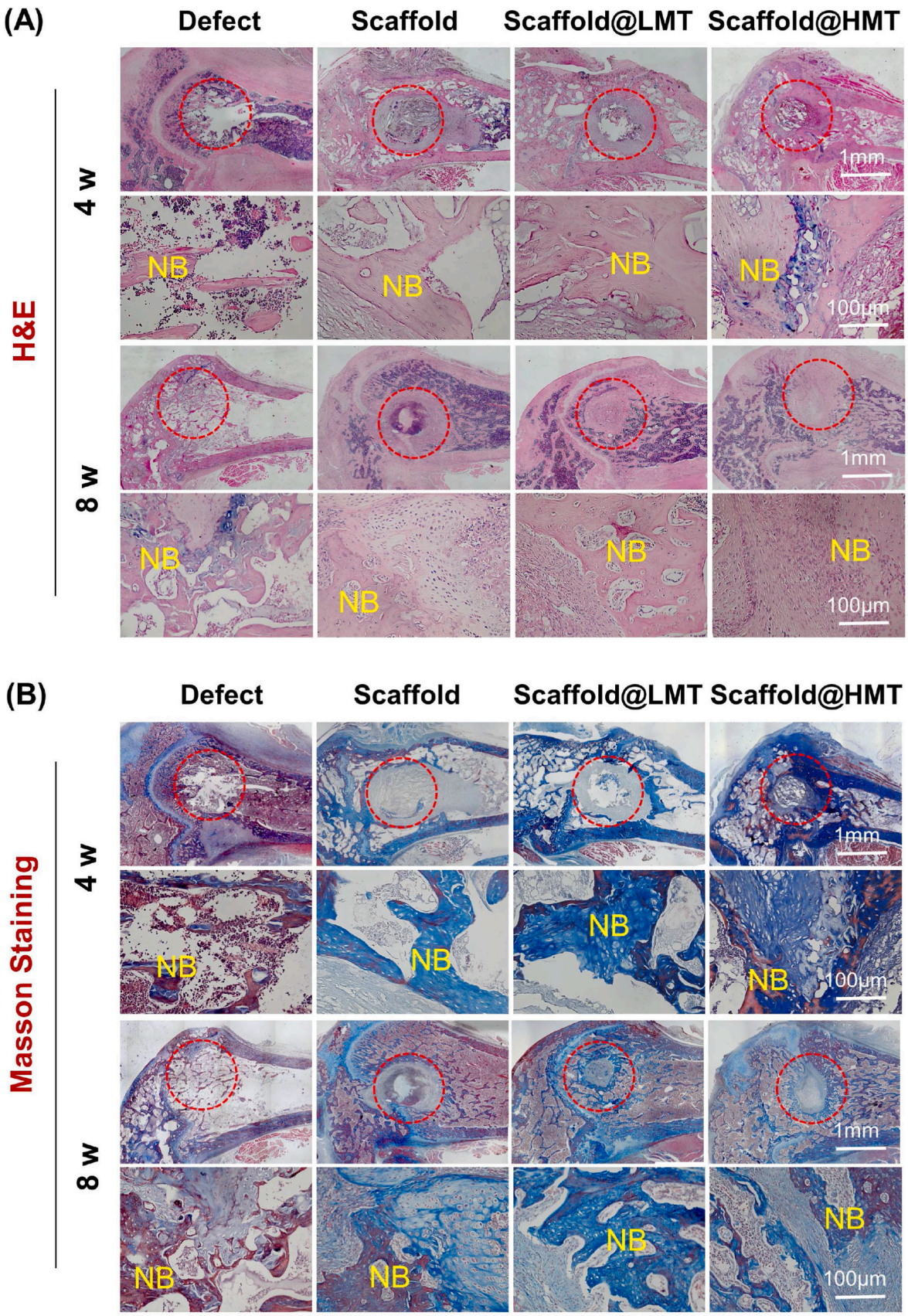

Fig. 8. Histological analysis of the newly formed bone tissue at 4 and 8 weeks post-surgery. (A) Representative hematoxylin and eosin (H&E) staining of the defect area implanted with nanofiber scaffolds loaded with melatonin. (B) Representative Masson staining of collagen deposition. Scale bar = 1 mm (upper panels). Scale bar = 100 μm (lower panels). NB: new bone.

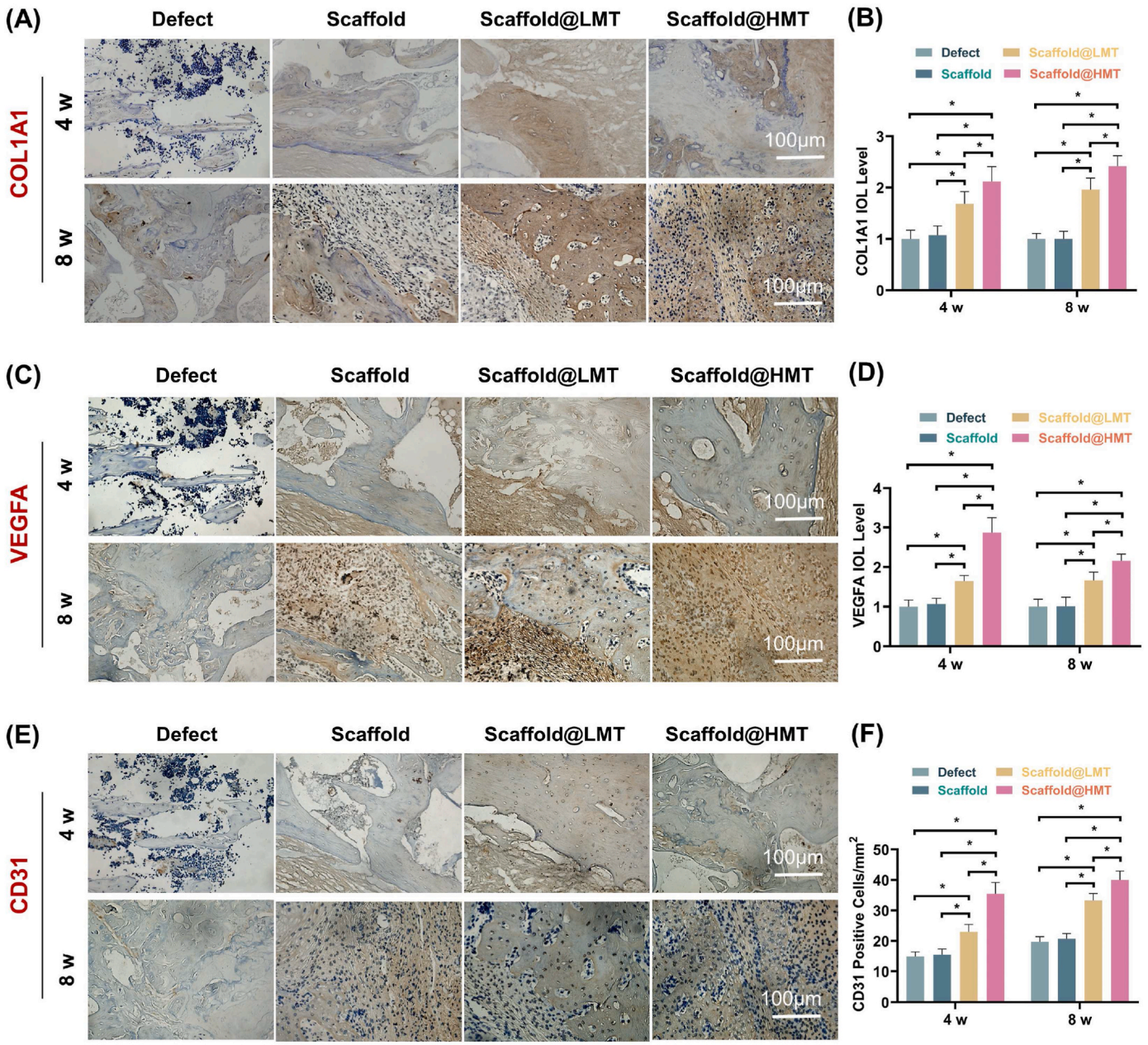

Fig. 9. Immunohistochemical analysis of the newly formed bone tissue and blood vessels. (A) Immunohistochemical staining for COL1A1 in the defect area. Scale bar = 100 μm. (B) Quantitative analysis of COL1A1-positive area at 4 and 8 weeks post-surgery, n = 3. (C) Immunohistochemical staining for VEGFA in the defect area. Scale bar = 100 μm. (D) Quantitative analysis of VEGFA-positive area at 4 and 8 weeks post-surgery, n = 3. (E) Immunohistochemical staining for CD31 in the defect area. Scale bar = 100 μm. (F) Quantitative analysis of the CD31-positive vessels at 4 and 8 weeks post-surgery, n = 3. Data are presented as means ± SEM. Statistically significant differences were indicated by * $P < 0.05$.

vascular endothelium. Notably, daily melatonin treatment effectively shielded HUVECs from oxidative stress, apoptosis, and mitochondrial damage. Consequently, this led to the restoration of aortic vasorelaxation and the release of nitric oxide in aged mice by activating the Sirtuin 3 antioxidant pathway [45]. Ragothaman et al. provided evidence that a collagen-based bio-hybrid hydrogel containing melatonin and silver nanoparticles facilitated prompt tissue regeneration and collagen deposition at the site of skin wounds by expediting the formation of blood vessels. This effect was primarily attributed to the synergistic interaction between melatonin and silver nanoparticles [46]. Consequently, we hypothesized that the utilization of melatonin-loaded electrospun nanofiber scaffolds in conjunction with BMMSCs undergoing osteogenesis could enhance the angiogenesis of HUVECs.

In this study, it was observed that the supernatant derived from Scaffold@HMT-cultured BMMSCs exhibited a significant enhancement in the migratory and tube-forming abilities of HUVECs. Additionally, the endothelial cells displayed heightened expression of CD31, a recognized marker for neovascularization, suggesting the potential angiogenic effect of Scaffold@HMT. Notably, Scaffold@HMT also upregulated the transcript and protein levels of VEGF in differentiated BMMSCs, which may be attributed to the augmented angiogenic response observed in HUVECs. In accordance with our findings, a prior investigation revealed that pre-treatment of BMMSCs with melatonin induced skin healing by upregulating the expression of VEGF in the wound area, thus presenting a more effective approach compared to BMMSC monotherapy [47]. Similarly, Zheng et al. demonstrated that melatonin treatment in a

laboratory setting enhanced the expression of markers associated with angiogenesis in BMMSCs, including VEGF, angiopoietin-2, and angiopoietin-4. Furthermore, *in vivo* experiments conducted on ovariectomized rats exhibited that melatonin administration expedited the repair of osteoporotic bones by stimulating bone mineralization and facilitating the formation of blood vessels around the tibia defect [48]. In order to elicit its protective effect, melatonin was integrated into an alginate-fibrin hydrogel, and concurrent administration with $CD144^{+}$ endothelial cells facilitated the development of neovascularization in cryopreserved/thawed ovaries transplanted into heterotopic rats, while preventing the deposition of fibrotic tissue [49]. Subsequent investigations will elucidate the fundamental mechanism through which melatonin-loaded nanofibers directly modulate the interplay between osteogenesis and angiogenesis by up-regulating the expression of VEGF during the process of bone regeneration.

To the best of our knowledge, this study represents the initial utilization of electrospun nanofiber-based sponge for the purpose of repairing femoral bone defects. The cultivation of human adipose tissue-derived MSCs on both aligned and randomly oriented ploy (L-lactide) (PLLA) electrospun nanofibers has been observed to enhance osteogenic differentiation, as indicated by elevated levels of ALP activity and extracellular calcium deposition. Furthermore, it has been discovered that the nanotopographical cues exert an influence on the bone morphogenetic protein (BMP) signaling pathway, with the electrospun nanofibers acting as a microRNA sponge that affects the expression of miR-125b, miR-15b, and miR-20a [50]. The present study successfully demonstrated that the inclusion of melatonin within nanofiber sponge-like scaffolds significantly enhanced the rate of bone healing in rat femurs. Furthermore, this intervention effectively stimulated the formation of neovascularization at the defect site, which plays a crucial role in sustaining bone metabolism through the provision of essential nutrients and oxygen, as well as the removal of waste products [51]. However, it is important to acknowledge that the absence of personalized design in the nanofibrous scaffold represents a limitation in this study, as clinical scenarios involve varying bone defects. To address this issue, the implementation of 3D printing technology offers a promising avenue for the development of tailored implants to effectively address individual bone defects. According to reports, the integration of electrospun nanofibers with a 3D-printed scaffold can be achieved through a layer-by-layer deposition technique. This integration of nanofibers and scaffold has been found to enhance the repair process of a calvarial defect by influencing the polarization of macrophages from M1 to M2 status. Consequently, this composite material has the ability to regulate the immune response within the bone defect environment [52]. Additionally, it is worth noting that bone reconstruction after complex trauma poses significant challenges in the field of orthopedic surgery. Liu et al. developed a biphasic hydrogel comprising two interconnected shape-tunable phases, enabling the controlled release of kartogenin and melatonin, known as chondrogenic and osteogenic inducers, respectively. This innovative approach effectively facilitated the simultaneous repair of articular cartilage and subchondral bone defects in a damaged joint [53]. Melatonin not only promotes osteoblast-driven bone formation [54,55], but also inhibits osteoclaster-mediated bone resorption [56]. Further investigation is warranted to determine the potential impact of a biomimetic nanofiber scaffold loaded with melatonin on osteoclasts during the bone repair process. Consequently, forthcoming research endeavors will focus on integrating electrospinning and 3D printing methodologies to incorporate melatonin alongside other osteogenic/angiogenic molecules, ultimately culminating in the successful functional restoration of bone defects.

5. Conclusions

In summary, a 3D electrospun nanofiber-based scaffold incorporating melatonin has been developed as an osteoinductive implant for bone defect repair. This sponge-like scaffold exhibits an interconnected porous structure with advantageous mechanical characteristics, facilitating cell proliferation and osteogenic differentiation of BMMSCs. Notably, their mitochondrial energy metabolism and antioxidant functions are enhanced when cultured with the melatonin-loaded nanofibrous scaffold, as indicated by elevated levels of ATP production, MMP, and respiratory chain factors. Additionally, the application of the supernatant obtained from Scaffold@HMT-cultured BMMSCs enhances the migratory and tube-forming capacities of HUVECs by facilitating VEGF secretion from BMMSCs. The results of *in vivo* experiments suggest that the implantation of a melatonin-loaded scaffold into bone defects in the distal femur of rats enhances bone matrix production and angiogenesis, thereby accelerating bone healing. Overall, these findings indicate that the transformation of 2D electrospun membranes into 3D nanofibrous scaffolds and their combination with melatonin may offer a promising strategy for facilitating bone regeneration.

CRediT authorship contribution statement

Nanning Lv: Writing – original draft, Formal analysis, Data curation, Conceptualization. **Mingzhuang Hou:** Writing – original draft, Formal analysis, Data curation, Conceptualization. **Lei Deng:** Writing – original draft, Data curation, Conceptualization. **Xi Hua:** Writing – original draft, Data curation. **Hao Liu:** Writing – review & editing, Formal analysis. **Xuesong Zhu:** Writing – review & editing, Methodology. **Yong Xu:** Writing – review & editing, Methodology. **Zhonglai Qian:** Writing – review & editing, Methodology. **Qing Li:** Writing – original draft, Methodology, Investigation, Funding acquisition. **Mingming Liu:** Writing – original draft, Supervision, Methodology, Funding acquisition. **Fan He:** Writing – review & editing, Writing – original draft, Supervision, Funding acquisition, Conceptualization.

Declaration of competing interest

The authors declare that they have no known competing financial interests or personal relationships that could have appeared to influence the work reported in this paper.

Data availability

Data will be made available on request.

Acknowledgements

This study was supported by the Natural Science Foundation of Jiangsu Province (BK20220046); Leading Talent of Changzhou "The 14th Five-Year Plan" High-level Health Personnel Training Project (2022260); Research Foundation of Kangda College of Nanjing Medical University (KD2022KYJJZD035); National Natural Science Foundation of China (82274558); Key Laboratory of Orthopaedics of Suzhou (SZS2022017); the Priority Academic Program Development of Jiangsu Higher Education Institutions (PAPD).

Appendix A. Supplementary data

Supplementary data to this article can be found online at https://doi.org/10.1016/j.mtbio.2024.101078.

References

[1] B. Baroli, From natural bone grafts to tissue engineering therapeutics: brainstorming on pharmaceutical formulative requirements and challenges, J Pharm Sci 98 (2009) 1317–1375.
[2] M. Zou, J. Sun, Z. Xiang, Induction of M2-type macrophage differentiation for bone defect repair via an interpenetration network hydrogel with a GO-based controlled release system, Adv. Healthcare Mater. 10 (2021) e2001502.
[3] W. Cheng, Z. Ding, X. Zheng, Q. Lu, X. Kong, X. Zhou, G. Lu, D.L. Kaplan, Injectable hydrogel systems with multiple biophysical and biochemical cues for bone regeneration, Biomater. Sci. 8 (2020) 2537–2548.

[4] J. Yin, G. Gong, C. Sun, Z. Yin, C. Zhu, B. Wang, Q. Hu, Y. Zhu, X. Liu, Angiopoietin 2 promotes angiogenesis in tissue-engineered bone and improves repair of bone defects by inducing autophagy, Biomed. Pharmacother. 105 (2018) 932–939.

[5] J. Song, X. Lin, L.Y. Ee, S.F.Y. Li, M. Huang, A review on electrospinning as versatile supports for diverse nanofibers and their applications in nnvironmental sensing, Adv Fiber Mater 5 (2023) 429–460.

[6] J. Xue, D. Pisignano, Y. Xia, Maneuvering the migration and differentiation of stem cells with electrospun nanofibers, Adv. Sci. 7 (2020) 2000735.

[7] J. Cui, X. Yu, B. Yu, X. Yang, Z. Fu, J. Wan, M. Zhu, X. Wang, K. Lin, Coaxially fabricated dual-drug loading electrospinning fibrous mat with programmed releasing behavior to boost vascularized bone regeneration, Adv. Healthcare Mater. 11 (2022) e2200571.

[8] B.A. Blakeney, A. Tambralli, J.M. Anderson, A. Andukuri, D.J. Lim, D.R. Dean, H. W. Jun, Cell infiltration and growth in a low density, uncompressed three-dimensional electrospun nanofibrous scaffold, Biomaterials 32 (2011) 1583–1590.

[9] L. Jin, Z.Q. Feng, M.L. Zhu, T. Wang, M.K. Leach, Q. Jiang, A novel fluffy conductive polypyrrole nano-layer coated PLLA fibrous scaffold for nerve tissue engineering, J. Biomed. Nanotechnol. 8 (2012) 779–785.

[10] Y. Chen, M. Shafiq, M. Liu, Y. Morsi, X. Mo, Advanced fabrication for electrospun three-dimensional nanofiber aerogels and scaffolds, Bioact. Mater. 5 (2020) 963–979.

[11] Y. Si, J. Yu, X. Tang, J. Ge, B. Ding, Ultralight nanofibre-assembled cellular aerogels with superelasticity and multifunctionality, Nat. Commun. 5 (2014) 5802.

[12] Y. Li, J. Wang, D. Qian, L. Chen, X. Mo, L. Wang, Y. Wang, W. Cui, Electrospun fibrous sponge via short fiber for mimicking 3D ECM, J. Nanobiotechnol. 19 (2021) 131.

[13] F. Munmun, P.A. Witt-Enderby, Melatonin effects on bone: implications for use as a therapy for managing bone loss, J. Pineal Res. 71 (2021) e12749.

[14] Y. Zhang, T. Liu, H. Yang, F. He, X. Zhu, Melatonin: a novel candidate for the treatment of osteoarthritis, Ageing Res. Rev. 78 (2022) 101635.

[15] K. Sharan, K. Lewis, T. Furukawa, V.K. Yadav, Regulation of bone mass through pineal-derived melatonin-MT2 receptor pathway, J. Pineal Res. 63 (2017) e12423.

[16] L. Zhou, X. Chen, J. Yan, M. Li, T. Liu, C. Zhu, G. Pan, Q. Guo, H. Yang, M. Pei, F. He, Melatonin at pharmacological concentrations suppresses osteoclastogenesis via the attenuation of intracellular ROS, Osteoporos. Int. 28 (2017) 3325–3337.

[17] W. Chen, X. Chen, A.C. Chen, Q. Shi, G. Pan, M. Pei, H. Yang, T. Liu, F. He, Melatonin restores the osteoporosis-impaired osteogenic potential of bone marrow mesenchymal stem cells by preserving SIRT1-mediated intracellular antioxidant properties, Free Radic. Biol. Med. 146 (2020) 92–106.

[18] Z. Yao, Y. Qian, Y. Jin, S. Wang, J. Li, W.E. Yuan, C. Fan, Biomimetic multilayer polycaprolactone/sodium alginate hydrogel scaffolds loaded with melatonin facilitate tendon regeneration, Carbohydr. Polym. 277 (2022) 118865.

[19] M. Hou, Y. Zhang, Y. Liu, X. Ge, X. Hu, Z. Zhao, X. Tian, T. Liu, H. Yang, X. Chen, F. He, X. Zhu, Biomimetic MT-loaded silk fibroin/GelMA scaffold strengthens cartilage repair through retrieval of mitochondrial functions, J. Mater. Sci. Technol. 146 (2023) 102–112.

[20] J. Liu, H. Zhou, W. Fan, W. Dong, S. Fu, H. He, F. Huang, Melatonin influences proliferation and differentiation of rat dental papilla cells in vitro and dentine formation in vivo by altering mitochondrial activity, J. Pineal Res. 54 (2013) 170–178.

[21] C.T. Chen, Y.R. Shih, T.K. Kuo, O.K. Lee, Y.H. Wei, Coordinated changes of mitochondrial biogenesis and antioxidant enzymes during osteogenic differentiation of human mesenchymal stem cells, Stem Cell. 26 (2008) 960–968.

[22] M.C. Wan, X.Y. Tang, J. Li, P. Gao, F. Wang, M.J. Shen, J.T. Gu, F. Tay, J.H. Chen, L.N. Niu, Y.H. Xiao, K. Jiao, Upregulation of mitochondrial dynamics is responsible for osteogenic differentiation of mesenchymal stem cells cultured on self-mineralized collagen membranes, Acta Biomater. 136 (2021) 137–146.

[23] I.M. Castano, R.M. Raftery, G. Chen, B. Cavanagh, B. Quinn, G.P. Duffy, C. M. Curtin, F.J. O'Brien, Dual scaffold delivery of miR-210 mimic and miR-16 inhibitor enhances angiogenesis and osteogenesis to accelerate bone healing, Acta Biomater. 172 (2023) 480–493.

[24] S. Zheng, C. Zhou, H. Yang, J. Li, Z. Feng, L. Liao, Y. Li, Melatonin accelerates osteoporotic bone defect repair by promoting osteogenesis-angiogenesis coupling, Front. Endocrinol. 13 (2022) 826660.

[25] S. Yildirimturk, S. Batu, C. Alatli, V. Olgac, D. Firat, Y. Sirin, The effects of supplemental melatonin administration on the healing of bone defects in streptozotocin-induced diabetic rats, J. Appl. Oral Sci. 24 (2016) 239–249.

[26] J.H. Lee, Y.S. Han, S.H. Lee, Potentiation of biological effects of mesenchymal stem cells in ischemic conditions by melatonin via upregulation of cellular prion protein expression, J. Pineal Res. 62 (2017) e12385.

[27] T. Zhao, J. Zhang, X. Gao, D. Yuan, Z. Gu, Y. Xu, Electrospun nanofibers for bone regeneration: from biomimetic composition, structure to function, J. Mater. Chem. B 10 (2022) 6078–6106.

[28] S. Anjum, F. Rahman, P. Pandey, D.K. Arya, M. Alam, P.S. Rajinikanth, Q. Ao, Electrospun biomimetic nanofibrous scaffolds: a promising prospect for bone tissue engineering and regenerative medicine, Int. J. Mol. Sci. 23 (2022) 9206.

[29] S. Nezamoleslami, A. Fattahi, H. Nemati, F. Bagrezaie, Z. Pourmanouchehri, S. H. Kiaie, Electrospun sandwich-structured of polycaprolactone/gelatin-based nanofibers with controlled release of ceftazidime for wound dressing, Int. J. Biol. Macromol. 236 (2023) 123819.

[30] Y. Mao, Y. Chen, W. Li, Y. Wang, J. Qiu, Y. Fu, J. Guan, P. Zhou, Physiology-inspired multilayer nanofibrous membranes modulating endogenous stem cell recruitment and osteo-differentiation for staged bone regeneration, Adv. Healthcare Mater. 11 (2022) e2201457.

[31] M. Mader, V. Jerome, R. Freitag, S. Agarwal, A. Greiner, Ultraporous, compressible, wettable polylactide/polycaprolactone sponges for tissue engineering, Biomacromolecules 19 (2018) 1663–1673.

[32] W. Guo, B. Zhao, M. Shafiq, X. Yu, Y. Shen, J. Cui, Y. Chen, P. Cai, Z. Yuan, M. El-Newehy, H. El-Hamshary, Y. Morsi, B. Sun, J. Pan, X. Mo, On the development of modular polyurethane-based bioelastomers for rapid hemostasis and wound healing, Regen Biomater 10 (2023) rbad019.

[33] S.Y. Lee, F. Long, Notch signaling suppresses glucose metabolism in mesenchymal progenitors to restrict osteoblast differentiation, J. Clin. Invest. 128 (2018) 5573–5586.

[34] W. Chen, D. Zheng, Y. Chen, H. Ruan, Y. Zhang, X. Chen, H. Shen, L. Deng, W. Cui, H. Chen, Electrospun fibers improving cellular respiration via mitochondrial protection, Small 17 (2021) e2104012.

[35] Q. Zhou, W. Chen, C. Gu, H. Liu, X. Hu, L. Deng, W. He, Y. Xu, X. Zhu, H. Yang, X. Chen, F. He, T. Liu, Selenium-modified bone cement promotes osteoporotic bone defect repair in ovariectomized rats by restoring GPx1-mediated mitochondrial antioxidant functions, Regen Biomater 10 (2023) rbad011.

[36] X. Qi, J. Wang, Melatonin improves mitochondrial biogenesis through the AMPK/PGC1alpha pathway to attenuate ischemia/reperfusion-induced myocardial damage, Aging (Albany NY) 12 (2020) 7299–7312.

[37] H. Jiang, X. Wang, X. Li, Y. Jin, Z. Yan, X. Yao, W.E. Yuan, Y. Qian, Y. Ouyang, A multifunctional ATP-generating system by reduced graphene oxide-based scaffold repairs neuronal injury by improving mitochondrial function and restoring bioelectricity conduction, Mater Today Bio 13 (2022) 100211.

[38] Y.H. Chan, K.N. Ho, Y.C. Lee, M.J. Chou, W.Z. Lew, H.M. Huang, P.C. Lai, S. W. Feng, Melatonin enhances osteogenic differentiation of dental pulp mesenchymal stem cells by regulating MAPK pathways and promotes the efficiency of bone regeneration in calvarial bone defects, Stem Cell Res. Ther. 13 (2022) 73.

[39] J.H. Son, Y.C. Cho, I.Y. Sung, I.R. Kim, B.S. Park, Y.D. Kim, Melatonin promotes osteoblast differentiation and mineralization of MC3T3-E1 cells under hypoxic conditions through activation of PKD/p38 pathways, J. Pineal Res. 57 (2014) 385–392.

[40] V. Alvarez-Garcia, A. Gonzalez, C. Alonso-Gonzalez, C. Martinez-Campa, S. Cos, Antiangiogenic effects of melatonin in endothelial cell cultures, Microvasc. Res. 87 (2013) 25–33.

[41] Q. Mu, M. Najafi, Modulation of the tumor microenvironment (TME) by melatonin, Eur. J. Pharmacol. 907 (2021) 174365.

[42] D. Sokolov, N. Sharda, B. Giri, M.S. Hassan, D. Singh, A. Tarasiewicz, C. Lohr, U. von Holzen, T. Kristian, J. Waddell, R.J. Reiter, H. Ahmed, A. Banerjee, Melatonin and andrographolide synergize to inhibit the colospheroid phenotype by targeting Wnt/beta-catenin signaling, J. Pineal Res. 73 (2022) e12808.

[43] S.J. Hwang, Y. Jung, Y.S. Song, S. Park, Y. Park, H.J. Lee, Enhanced anti-angiogenic activity of novel melatonin-like agents, J. Pineal Res. 71 (2021) e12739.

[44] S.C. Liu, C.H. Tsai, Y.H. Wang, C.M. Su, H.C. Wu, Y.C. Fong, S.F. Yang, C.H. Tang, Melatonin abolished proinflammatory factor expression and antagonized osteoarthritis progression in vivo, Cell Death Dis. 13 (2022) 215.

[45] F.Y. Lee, C.K. Sun, P.H. Sung, K.H. Chen, S. Chua, J.J. Sheu, S.Y. Chung, H.T. Chai, Y.L. Chen, T.H. Huang, C.R. Huang, Y.C. Li, C.W. Luo, H.K. Yip, Daily melatonin protects the endothelial lineage and functional integrity against the aging process, oxidative stress, and toxic environment and restores blood flow in critical limb ischemia area in mice, J. Pineal Res. 65 (2018) e12489.

[46] M. Ragothaman, A. Kannan Villalan, A. Dhanasekaran, T. Palanisamy, Bio-hybrid hydrogel comprising collagen-capped silver nanoparticles and melatonin for accelerated tissue regeneration in skin defects, Mater. Sci. Eng., C 128 (2021) 112328.

[47] A.M. Al-Otaibi, A.S. Al-Gebaly, R. Almeer, G. Albasher, W.S. Al-Qahtani, A.E. Abdel Moneim, Melatonin pre-treated bone marrow derived-mesenchymal stem cells prompt wound healing in rat models, Biomed. Pharmacother. 145 (2022) 112473.

[48] L. Chen, R.Y. Zhang, J. Xie, J.Y. Yang, K.H. Fang, C.X. Hong, R.B. Yang, N. Bsoul, L. Yang, STAT3 activation by catalpol promotes osteogenesis-angiogenesis coupling, thus accelerating osteoporotic bone repair, Stem Cell Res. Ther. 12 (2021) 108.

[49] M. Izadpanah, A.R. Del Bakhshayesh, Z. Bahroudi, A.M. Seghinsara, R. Beheshti, M. Mahdipour, M.R. Zarnaghi, P. Hassanpour, N. Mardi, R. Rahbarghazi, A. Abedelahi, Melatonin and endothelial cell-loaded alginate-fibrin hydrogel promoted angiogenesis in rat cryopreserved/thawed ovaries transplanted to the heterotopic sites, J. Biol. Eng. 17 (2023) 23.

[50] M. Izadpanahi, E. Seyedjafari, E. Arefian, A. Hamta, S. Hosseinzadeh, M. Kehtari, M. Soleimani, Nanotopographical cues of electrospun PLLA efficiently modulate non-coding RNA network to osteogenic differentiation of mesenchymal stem cells during BMP signaling pathway, Mater. Sci. Eng., C 93 (2018) 686–703.

[51] S. Jin, R. Yang, C. Chu, C. Hu, Q. Zou, Y. Li, Y. Zuo, Y. Man, J. Li, Topological structure of electrospun membrane regulates immune response, angiogenesis and bone regeneration, Acta Biomater. 129 (2021) 148–158.

[52] X. Liu, M. Chen, J. Luo, H. Zhao, X. Zhou, Q. Gu, H. Yang, X. Zhu, W. Cui, Q. Shi, Immunopolarization-regulated 3D printed-electrospun fibrous scaffolds for bone regeneration, Biomaterials 276 (2021) 121037.

[53] X. Liu, Y. Chen, A.S. Mao, C. Xuan, Z. Wang, H. Gao, G. An, Y. Zhu, X. Shi, C. Mao, Molecular recognition-directed site-specific release of stem cell differentiation inducers for enhanced joint repair, Biomaterials 232 (2020) 119644.

[54] F. Malakoti, F. Zare, R. Zarezadeh, A. Raei Sadigh, A. Sadeghpour, M. Majidinia, B. Yousefi, F. Alemi, The role of melatonin in bone regeneration: a review of involved signaling pathways, Biochimie 202 (2022) 56–70.
[55] Y. Zhou, C. Wang, J. Si, B. Wang, D. Zhang, D. Ding, J. Zhang, H. Wang, Melatonin up-regulates bone marrow mesenchymal stem cells osteogenic action but suppresses their mediated osteoclastogenesis via MT(2) -inactivated NF-kappaB pathway, Br. J. Pharmacol. 177 (2020) 2106–2122.
[56] I.J. MacDonald, H.C. Tsai, A.C. Chang, C.C. Huang, S.F. Yang, C.H. Tang, Melatonin inhibits osteoclastogenesis and osteolytic bone metastasis: implications for osteoporosis, Int. J. Mol. Sci. 22 (2021) 9435.